

# Spectral Gating Networks

Jusheng Zhang<sup>1,2</sup> Yijia Fan<sup>1</sup> Kaitong Cai<sup>1</sup> Jing Yang<sup>1</sup>  
 Yongsen Zheng<sup>2</sup> Kwok-Yan Lam<sup>2</sup> Liang Lin<sup>1</sup> Keze Wang<sup>1</sup>

## Abstract

Gating mechanisms are ubiquitous, yet a complementary question in feed-forward networks remains under-explored, i.e., how to introduce frequency-rich expressivity without sacrificing stability and scalability? This tension is exposed by spline-based Kolmogorov–Arnold Network (KAN) parameterizations, where grid refinement can induce parameter growth and brittle optimization in high dimensions. To propose a stability-preserving way to inject spectral capacity into existing MLP/FFN layers under fixed parameter and training budgets, we introduce *Spectral Gating Networks (SGN)*, a drop-in spectral reparameterization. Our SGN augments a standard activation pathway with a compact spectral pathway and learnable gates that allow the model to start from a stable base behavior and progressively allocate capacity to spectral features during training. The spectral pathway is instantiated with trainable Random Fourier Features (learned frequencies and phases), replacing grid-based splines and removing resolution dependence. A hybrid GELU-Fourier formulation further improves optimization robustness while enhancing high-frequency fidelity. Across vision, NLP, audio, and PDE benchmarks, SGN consistently improves accuracy-efficiency trade-offs under comparable computational budgets, achieving **93.15%** accuracy on CIFAR-10 and up to **11.7 $\times$**  faster inference than spline-based KAN variants. Code and trained models will be released.

## 1. Introduction

Spectral gating is well-established in neural networks, but its role inside feed-forward networks (MLP) (Rumelhart et al., 1986; Vaswani et al., 2023; Rahaman et al., 2019;

<sup>1</sup>Sun Yat-sen University, China <sup>2</sup>Nanyang Technological University, Singapore. Correspondence to: Keze Wang <keze-wang@gmail.com>.

Preprint. February 10, 2026.

John Xu et al., 2020a) remains surprisingly under-examined. Early architectures introduced learnable nonlinearity shaping through fixed activations and gating, and modern models continue to rely on FFN blocks as the primary source of feature transformation and capacity (Srivastava et al., 2015; Dauphin et al., 2017; Zhang et al., 2023; Vaswani et al., 2023; John Xu et al., 2020b). In parallel, learnable basis parameterizations—ranging from spline families to Fourier-feature representations—have been repeatedly proposed to enhance expressiveness, especially for capturing high-frequency components (Unser, 1999; Tancik et al., 2020). Despite widespread adoption and empirical success, the function and impact of “spectral capacity injection” in FFNs are still insufficiently understood beyond intuition, making it hard to assess what truly drives improvements once it is entangled with other architectural changes.

Insufficient understanding is especially problematic when basis changes are confounded with other factors (Bengio et al., 2014; John Xu et al., 2020b). For instance, spline-parameterized designs inspired by Kolmogorov–Arnold Networks (Liu et al., 2025; 2024) may report stronger approximation, yet their performance and efficiency often covary with grid resolution, parameter growth, normalization choices, and optimization recipes, i.e., making it unclear whether gains come from the spline basis itself or from accompanying design or engineering decisions. Similarly, Fourier-feature augmentations can improve spectral expressiveness, but are frequently introduced together with width or depth changes, normalization, or task-specific tuning, which again obscures the contribution of the spectral representation. These considerations underscore the need to rigorously disentangle the effects of spectral expressivity from stability and scaling factors in FFNs, and to identify the minimal modification that yields consistent benefits across settings. In this work, we investigate spectral gating mechanisms in standard FFNs. Specifically, we introduce a **Spectral Gating Network (SGN)** module (Rumelhart et al., 1986; Schmidhuber, 2015) (formally defined in Eq. 2, Sec. 3) that augments a conventional FFN with an additional compact spectral pathway and a learnable gate that controls information flow between pathways. Our exploration covers SGN variants along several key aspects: (1) spectral bases (fixed vs. trainable Random Fourier Features;

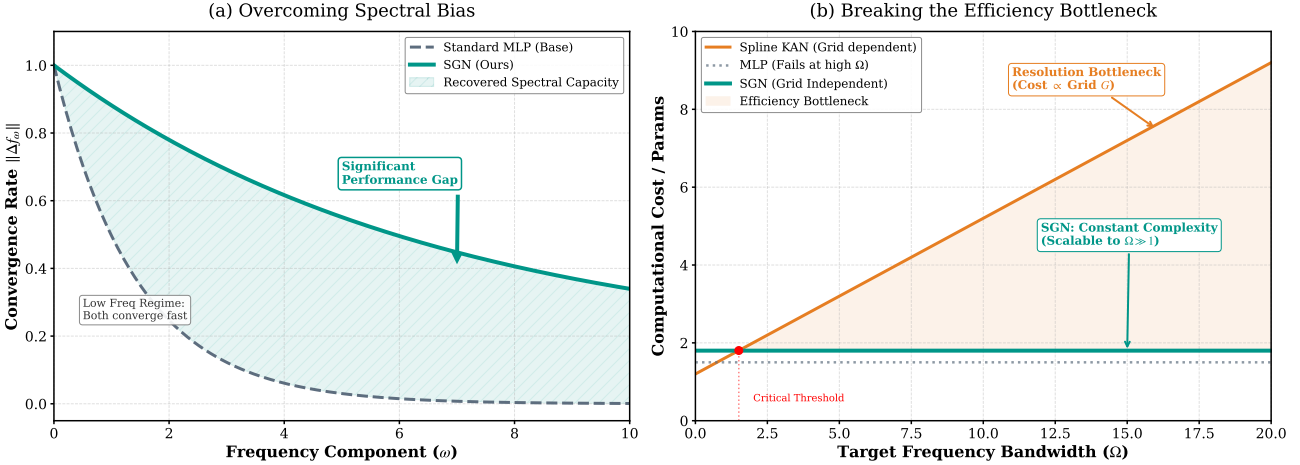


**Figure 1. Conceptual illustration and theoretical analysis of the Spectral-Efficiency gap.** (a) **Overcoming Spectral Bias:** Illustrating Problem 1. Standard MLPs (grey dashed) suffer from exponential convergence decay as frequency  $\omega$  increases, creating a "spectral gap" (hatched area). SGN (green solid) maintains robust learnability across the spectrum. (b) **Breaking the Efficiency Bottleneck:** Illustrating Problem 2. While spline-based KANs (orange) incur linear cost scaling with grid resolution  $G$  (creating an efficiency bottleneck at high  $\Omega$ ), SGN maintains constant complexity, effectively enabling scalable high-frequency modeling.

learned frequencies and phases), (2) gating forms (additive vs. multiplicative; scalar vs. channel-wise), and (3) stabilization strategies (where and how to normalize the spectral branch; how to initialize gates to preserve a stable "base FFN" regime). The exploration results demonstrate that: (i) a gated spectral augmentation is consistently beneficial, and the most reliable configuration is one that keeps the original activation pathway intact while letting the spectral branch be introduced progressively via a learnable gate; (ii) SGN substantially improves the accuracy–efficiency trade-off across modalities, achieving strong performance under comparable budgets while avoiding the grid-resolution–driven parameter and latency overhead that often arises in spline-table parameterizations (see theoretical complexity in **Theorem 3.2**).

We identify two primary factors contributing to SGN’s effectiveness. (i) **Stability-preserving decoupling.** The gate decouples "optimization-friendly behavior" from "spectral capacity." By implementing a **continuation principle** (analyzed in **Theorem 3.1**), the FFN starts from a stable base behavior and only allocates additional spectral expressivity when optimization supports it, preventing early-training brittleness that commonly accompanies aggressive basis replacement. (ii) **Adaptive spectral expressiveness.** Allowing the spectral branch to learn task-dependent frequencies and phases concentrates capacity on relevant bands, improving high-frequency fidelity without requiring grid refinement or large parameter tables. Together, these factors explain why SGN acts as a minimal, architecture-compatible modification that reliably improves both performance and scalability.

In summary, our study highlights the intrinsic value of spectral gating inside FFNs. By systematically evaluating SGN variants and isolating confounding factors, we show that a

simple gated spectral augmentation can deliver consistent gains across vision, language, audio, and partial differential equation (PDE) tasks (comprehensive results in **Sec. 4**), while remaining close to MLP-level runtime.

## 2. Problem Formulation: The Spectral-Efficiency Gap

In this section, we formalize the fundamental limitations of standard Feed-Forward Networks (FFNs (Rumelhart et al., 1986; Rahaman et al., 2019)) in capturing high-frequency features, and analyze why recent spline-based alternatives (e.g., KAN-style parameterizations) do not yet provide a scalable drop-in solution for large backbones.

**Setup.** Consider a standard FFN layer, the backbone of modern Transformers. Given an input token  $x \in \mathbb{R}^{d_{\text{model}}}$ , the FFN computes:

$$u = W_1 x + b_1, \quad y = W_2 \phi(u) + b_2, \quad (1)$$

where  $W_1 \in \mathbb{R}^{d_{\text{ff}} \times d_{\text{model}}}$ ,  $W_2 \in \mathbb{R}^{d_{\text{model}} \times d_{\text{ff}}}$ , and  $\phi(\cdot)$  is a fixed element-wise nonlinearity (e.g., GELU). While efficient and stable, this parameterization faces a critical dilemma: improving high-frequency expressivity typically comes at the cost of either (i) scaling depth/width aggressively, or (ii) adopting alternative parameterizations that break hardware efficiency and warm-start compatibility.

**Problem 1: The Intrinsic Spectral Bias of MLPs.** The primary bottleneck of standard FFNs is their difficulty in efficiently learning high-frequency components. As characterized by the *Frequency Principle*, gradient-based training of standard MLPs tends to fit low-frequency components earlier and more reliably than high-frequency ones. Concretely,

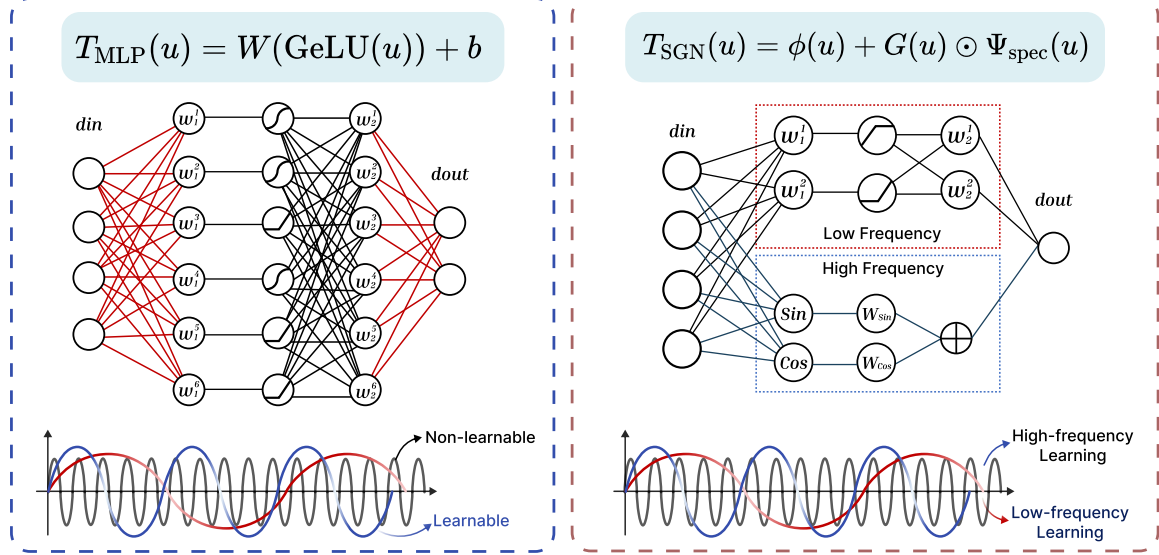


**Figure 2. Architecture Comparison: MLP vs. SGN.** (Left) A standard MLP layer relies on global weights and fixed activations, primarily capturing low-frequency components. (Right) The proposed SGN architecture introduces a parallel **Spectral Branch**. Features are split into a stable low-frequency path (Base Activation) and a high-frequency path (Sine/Cosine modulations via RFF). A learnable gate adaptively combines the two branches, achieving expressive detail modeling without sacrificing MLP stability.

consider a target function  $f$  with Fourier spectrum  $\hat{f}(\omega)$ . For many common activations, the optimization dynamics exhibit a convergence behavior whose effective speed degrades as  $\|\omega\|$  grows (**visualized in Fig. 1a**). This implies that components at large  $\|\omega\|$  are learned late or remain underfit within a practical compute budget (Rahaman et al., 2019; John Xu et al., 2020a; Poggio et al., 2018).

This spectral bias becomes a practical issue in tasks where fine-grained details are essential (e.g., textures in vision, or high-frequency oscillations in PDE solving) (Geirhos et al., 2022). In such cases, a standard FFN often compensates by excessively scaling depth or width, resulting in over-parameterized models that are still prone to underfitting high-frequency content.

**Problem 2: The Resolution-Efficiency Bottleneck of Spline-based Solutions.** A natural response to spectral bias is to introduce learnable function bases with higher local flexibility, such as KANs (Liu et al., 2025), which replace fixed activations with learnable splines defined over a grid of resolution  $G$ . While expressive, they introduce a severe **Resolution-Efficiency Trade-off** (**analyzed in Fig. 1b**):

- **Channel-wise Scaling:** Even for simple 1D splines, the cost scales as  $O(d_{ff} \cdot G)$ . This couple's high-frequency capacity directly to grid resolution.
- **Hardware Inefficiency:** Spline evaluation often incurs irregular memory access (lookup/interpolation), significantly reducing throughput on modern accelerators compared to dense GEMM operations.

Consequently, spline-based alternatives are challenging to deploy as universally scalable drop-in replacements for FFNs in large-scale backbones.

**Our Goal.** We aim to design a **universal FFN reparameterization** that resolves spectral bias *without* incurring the efficiency penalties of spline grids. Specifically, we seek an operator  $\mathcal{T}(u)$  such that: **High-Frequency Capability:** Overcome MLP spectral bias and efficiently model bandwidth  $\Omega \gg 1$ . **MLP-Level Efficiency:** Maintain hardware-friendly dense linear algebra with complexity linear in  $d_{ff}$ , strictly independent of grid resolution. **Warm-Start Compatibility:** Admit a stable initialization where  $\mathcal{T}(u) \approx \phi(u)$ , inheriting the optimization landscape of pre-trained FFNs to avoid cold-start instability.

### 3. Spectral Gating Networks (SGN)

To achieve the goals in Sec. 2, we propose **Spectral Gating Networks (SGN)**. Unlike spline-based replacements that *discard* the standard activation (sacrificing stability) (Bohra et al., 2020; Scardapane et al., 2018), SGN **augments** the standard FFN. We treat the base MLP as a stable low-frequency learner and inject a lightweight, gated spectral branch to learn high-frequency residuals (He et al., 2016).

#### 3.1. Formulation

**Core Formulation.** We redefine the FFN activation path in Eq. (1) as a hybrid composition. For the latent feature

$u \in \mathbb{R}^{d_{\text{ff}}}$ , SGN computes:

$$\mathcal{T}_{\text{SGN}}(u) = \underbrace{\phi(u)}_{\text{Base MLP Branch}} + \underbrace{\mathcal{G}(u) \odot \Psi_{\text{spec}}(u)}_{\text{Spectral Branch}}, \quad (2)$$

where  $\phi(u)$  is the standard activation (preserving pretrained behavior),  $\Psi_{\text{spec}}(u)$  is an adaptive spectral mapping, and  $\mathcal{G}(u)$  is a learnable gate. Note that, unlike prior spectral or spline-based designs that replace the base activation, our SGN preserves the original FFN pathway and restricts the spectral component to a gated residual, which is critical for stability in pretrained or deep architectures.

This design directly addresses the problems in Sec. 2: **Solving Problem 1 (Spectral Bias):** The mapping  $\Psi_{\text{spec}}$  provides an explicit pathway for high-frequency gradients that fixed  $\phi(\cdot)$  tends to suppress (Tancik et al., 2020). **Solving Problem 2 (Efficiency):** We parameterize  $\Psi_{\text{spec}}$  via dense Fourier features rather than grids, decoupling expressivity from resolution  $G$  and preserving GEMM-friendly computation.

### Theorem 3.1 (Homotopy Consistency & Cold-Start Stability).

Let the FFN output be  $y = W_2 \mathcal{T}(u) + b_2$ . Consider SGN with  $\mathcal{T}_{\text{SGN}}$  in Eq. (2). If the spectral branch is initialized with negligible magnitude (e.g.,  $A_r \sim \mathcal{N}(0, \epsilon^2)$ ), then at initialization:

$$\begin{aligned} \mathcal{T}_{\text{SGN}}^{(0)}(u) &= \phi(u) + O(\epsilon), \\ \nabla_{\theta_{\text{base}}} \mathcal{L}_{\text{SGN}}^{(0)} &= \nabla_{\theta_{\text{base}}} \mathcal{L}_{\text{MLP}}^{(0)} + O(\epsilon), \\ \|\nabla_{\theta_{\text{spec}}} \mathcal{L}_{\text{SGN}}^{(0)}\| &= O(\epsilon), \end{aligned} \quad (3)$$

where  $\theta_{\text{spec}} = \{W_r, b_r, A_r, w_g, b_g\}$ . This homotopy-style initialization guarantees that SGN inherits the robust optimization behavior of the pretrained FFN, avoiding the cold-start instability of pure spectral replacements. See Appendix H for the complete proof.

**Lightweight Channel-wise Gating.** To ensure SGN remains efficient, we employ **channel-wise gating**:

$$\mathcal{G}(u) = \sigma(w_g \odot \text{LN}(u) + b_g), \quad (4)$$

where  $w_g, b_g \in \mathbb{R}^{d_{\text{ff}}}$  and LN denotes LayerNorm. This adds negligible parameter overhead:  $2d_{\text{ff}}$  parameters for  $(w_g, b_g)$ , plus an optional  $2d_{\text{ff}}$  if LayerNorm uses affine parameters  $(\gamma, \beta)$ , which still remains  $O(d_{\text{ff}})$ . In contrast, full-matrix gating would incur  $O(d_{\text{ff}}^2)$  parameters, while our design preserves the per-channel adaptivity crucial for selective spectral injection.

**Spectral Branch via Trainable RFF.** We instantiate  $\Psi_{\text{spec}}$  using **Trainable Random Fourier Features (RFF)**.

Let  $m$  be a fixed *spectral budget*. We define the feature map:

$$\gamma(u) = \sqrt{\frac{2}{m}} \left[ \cos(W_r^\top u + b_r) \oplus \sin(W_r^\top u + b_r) \right], \quad (5)$$

where  $W_r \in \mathbb{R}^{d_{\text{ff}} \times m}$  and  $b_r \in \mathbb{R}^m$ . The spectral output is projected back to  $\mathbb{R}^{d_{\text{ff}}}$ :

$$\Psi_{\text{spec}}(u) = \gamma(u) A_r, \quad A_r \in \mathbb{R}^{2m \times d_{\text{ff}}}. \quad (6)$$

We initialize  $W_r \sim \mathcal{N}(0, \sigma^2)$  to match a target bandwidth. Crucially, by *learning*  $W_r$ , SGN adapts its spectral receptive field to the data distribution, achieving high-frequency fidelity without parameter explosion.

### 3.2. Theoretical Analysis

We analyze how SGN preserves stability while expanding spectral capacity. **Analysis: Gradient Modulation & Spectral Expansion.** To explain the mechanism, we decompose the Jacobian  $J_{\mathcal{T}}(u)$  using the product rule:

$$J_{\mathcal{T}}(u) = \underbrace{\text{diag}(\phi'(u))}_{\text{Base Term}} + \underbrace{\text{diag}(\mathcal{G}(u)) J_{\Psi_{\text{spec}}}(u)}_{\text{Spectral Injection}} + \underbrace{\text{diag}(\Psi_{\text{spec}}(u)) J_{\mathcal{G}}(u)}_{\text{Gate Modulation}} \quad (7)$$

Standard FFNs are limited by the *Base Term*, which typically smooths high frequencies. SGN introduces the *Spectral Injection* term, routing gradients through Fourier features to learn fine details. The gate  $\mathcal{G}(u)$  ensures this injection is localized and stable.

### Theorem 3.2 (Proposition: Spectral Bandwidth Expansion).

Let  $\mathcal{B}_\phi$  be the effective spectral bandwidth of the base activation. Let  $\{\omega_j\}_{j=1}^m$  denote the columns of  $W_r$ . SGN extends the representable bandwidth to  $\mathcal{B}_\phi \cup \{\omega_j\}_{j=1}^m$ . By learning  $W_r$ , SGN effectively performs kernel density estimation in the frequency domain, dynamically allocating capacity to task-relevant frequencies. **The rigorous basis containment proof is provided in Appendix H.4.**

**Theorem 3.3 (Linear Complexity (MLP-Level Efficiency)).** Let  $m$  be the fixed spectral budget. The parameter overhead of SGN relative to a standard FFN is:

$$\begin{aligned} \Delta P_{\text{SGN}} &= \underbrace{(d_{\text{ff}} + 1)m}_{W_r, b_r} + \underbrace{2md_{\text{ff}}}_{A_r} + \underbrace{2d_{\text{ff}}}_{\text{Gate}} \\ &= O(d_{\text{ff}}m) + O(d_{\text{ff}}). \end{aligned} \quad (8)$$

Critically, for a fixed small constant  $m \ll d_{\text{ff}}$ , SGN remains **linear** in  $d_{\text{ff}}$  and preserves hardware-friendly dense operations, contrasting with the grid-dependent scaling of KANs. **Detailed derivations and FLOPs analysis are given in Appendix I.**

**Table 1. Design space exploration of SGN.** We compare against baselines including Standard FFN and Spline-based KANs. ‘Params’ denotes relative parameter count vs. Standard FFN. **Bold** indicates best performance.

Method	Gate Pos.	Granularity	Basis Type	Params	Acc
<b>Baselines</b>					
(1) Standard FFN	–	–	GELU	1.0×	78.5
(2) KAN (Spline)	–	–	B-Spline	3.5×	79.2
<b>SGN Variants (Ours)</b>					
(3) SGN (Pre-Act)	$u$	Channel	Train RFF	1.1×	79.8
(4) SGN (Post-Mix)	$\phi + \psi$	Channel	Train RFF	1.1×	80.1
(5) <b>SGN (Spectral)</b>	$\Psi_{\text{spec}}$	<b>Channel</b>	<b>Train RFF</b>	<b>1.1×</b>	<b>81.5</b>
(6) SGN (Scalar)	$\Psi_{\text{spec}}$	Layer-wise	Train RFF	1.05×	79.0
(7) SGN (Fixed)	$\Psi_{\text{spec}}$	Channel	Fixed RFF	1.1×	80.2
(8) SGN (Additive)	$\Psi_{\text{spec}}$	Channel	Train RFF	1.1×	80.5

### 3.3. Design Analyses

We systematically evaluate SGN design choices to confirm the superiority of the hybrid gated architecture. As shown in Table 1, our SGN (Row 5) significantly outperforms the Standard FFN (Row 1), supporting the thesis that overcoming spectral bias yields measurable gains. Crucially, SGN also outperforms the spline baseline (Row 2) while using far fewer parameters ( $1.1\times$  vs  $3.5\times$ ), validating our solution to the Resolution-Efficiency bottleneck.

## 4. Experiments

The objective of this experiment is to evaluate the performance of mainstream models when their MLP (Rumelhart et al., 1986) or KAN (Liu et al., 2025) components are replaced with **SGN**. By maintaining consistent parameters, we conducted experiments across a variety of tasks, including simple visual tasks, NLP tasks, audio tasks, and machine learning tasks, utilizing models such as ResNet-18 (He et al., 2015), DeiT (Touvron et al., 2021) (from the MLP-KAN architecture), MLPmixer (Berner et al., 2022), and GPT-2 (Brown et al., 2020). Additionally, we tested the performance of SGN in function fitting (see Appendix D.2.1) and solving differential equations (see Appendix D.2.2). We also compared SGN with Methods Addressing Spectral Bias, and the experimental results showed that we still maintain the best performance (see Appendix E.5). We test KAN using the pykan repository. In particular, we call `model.speed()` to disable symbolic branching to ensure fair experiments. All experiments employed either the Adam (Kingma & Ba, 2014) optimizer, with learning rates appropriately selected according to the specific task. The experimental environment is set up with RTX 4090 GPUs.

### 4.1. Comprehensive Evaluation Based on Kanbefair

Based on Kanbefair (Yu et al., 2024), we conduct a comprehensive evaluation of SGN on vision (Dosovitskiy et al., 2021), NLP (Brown et al., 2020), audio, and machine learn-

ing tasks to compare its performance with existing models. We selected MLP (with GELU activation), KAN, FAN (Dong et al., 2024), and GPKAN (Yang & Wang, 2024).

**Experimental Setup.** All models are trained for 40 epochs. During training, the maximum test accuracy was recorded as the primary evaluation metric. For **SGN**, the key parameters included a spectral budget matching the parameter constraints, an activation expectation of 1.64, and GELU as the base activation function. For KAN, we used a grid extension to ensure fair comparison. For MLP, we experimented with both GELU (Hendrycks & Gimpel, 2016) and ReLU (Nair & Hinton, 2010; Glorot et al., 2011) activations. FAN’s `p_ratio` was set to 0.25, and GPKAN used GELU-based initialization. We also provide T-tests in the Supp. E.4 to increase the statistical rigor.

**Experimental Results.** As shown in Figure 3 and Table 2, we have conducted a systematic comparison. The results demonstrate that SGN consistently achieves the highest accuracy under the same parameter settings. Analysis. This performance gap is particularly pronounced on datasets rich in high-frequency textures, such as CIFAR-10 and SVHN. Standard MLPs, constrained by the “spectral bias” of smooth activations (e.g., GELU), struggle to capture these fine-grained patterns without excessive depth. SGN overcomes this by explicitly allocating a portion of its capacity to the spectral branch, effectively acting as a high-pass filter that complements the low-frequency bias of the base branch. Furthermore, unlike GPKAN, which exhibits training instability (reflected in its varying performance across datasets), SGN’s gated initialization ensures a stable optimization trajectory, matching the robustness of standard MLPs while exceeding their expressivity. In addition to vision tasks, Figure 4 (see Appendix D.1) evaluates SGN’s performance on NLP, audio, and ML datasets, where SGN also achieves superior results.

### 4.2. Experiments on Complex Vision Models

To comprehensively evaluate SGN in large-scale vision models, we assess its impact on accuracy, computation time, and generalization. We replace the original MLP or KAN layers in architectures, including ResNet-18, ViT-Tiny, MLP-Mixer-S/16, and MLP\_KAN (DeiT-based) with SGN, and report consistent gains under both constraint-controlled and strong-tuning regimes.

**Experimental Setup.** We evaluate on CIFAR-10, CIFAR-100 (Krizhevsky et al., 2009), and ImageNet-1K. For each backbone, we conduct experiments under two settings: (1) a *Standard Setting* that uses fixed hyperparameters and minimal tuning for fair architectural comparison (reported in Table 2); and (2) an *Optimized Setting* that adopts a stronger recipe (e.g., Mixup/CutMix and improved schedules) to probe the accuracy frontier. Crucially, to avoid confounding

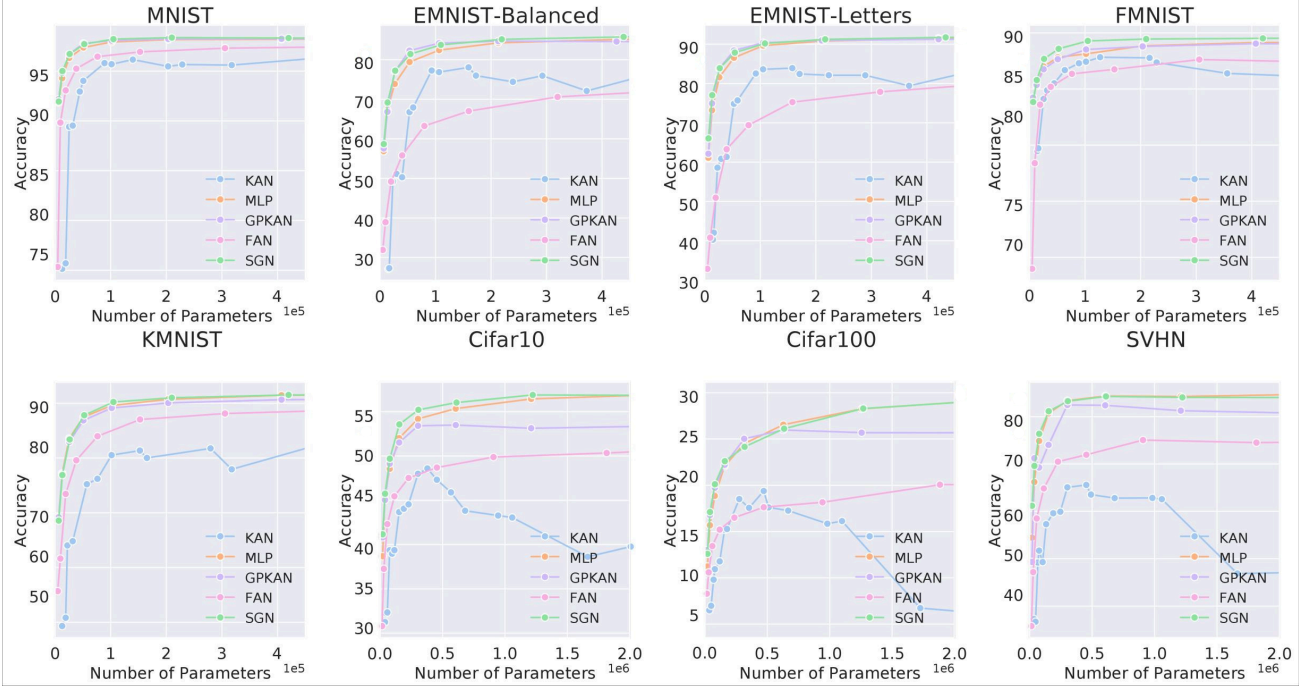


Figure 3. Performance comparison of different models (KAN, MLP, GPKAN, FAN, SGN) on simple networks across multiple datasets. The results show that SGN typically achieves higher accuracy with fewer parameters.

Table 2. Comprehensive comparison of different models on various datasets. Blue rows indicate our method (SGN).

Model	Datasets	Mixer	#Param.	FLOPs	Top-1	Model	Datasets	Mixer	#Param.	FLOPs	Top-1
ResNet/18	CIFAR-10	MLP	11.1M	0.56G	91.19	MLP_Mixer/S	ImageNet1k	MLP	18.2M	3.8G	63.5
ResNet/18	CIFAR-10	SGN	12.0M	0.63G	<b>91.72</b>	MLP_Mixer/S	ImageNet1k	SGN	18.8M	4.2G	<b>64.7</b>
ResNet/18	CIFAR-10	GPKAN	11.3M	0.56G	90.98	MLP_Mixer/S	ImageNet1k	GPKAN	18.8M	4.0G	62.9
ResNet/18	CIFAR-10	FAN	8M	0.42G	90.69	MLP_Mixer/S	ImageNet1k	FAN	15.7M	3.2G	58.2
ResNet/18	CIFAR-10	KAN	Too large	–	–	MLP_Mixer/S	ImageNet1k	KAN	Too large	–	–
ViT-T/16	ImageNet1K	MLP	5.7M	1.08G	72.3	MLP_KAN	Cifar100	MLP	1.3M	0.12G	49.0
ViT-T/16	ImageNet1K	SGN	5.9M	1.12G	<b>73.2</b>	MLP_KAN	Cifar100	SGN	1.4M	0.15G	<b>53.8</b>
ViT-T/16	ImageNet1K	GPKAN	5.7M	1.13G	74.6	MLP_KAN	Cifar100	KAN	1.9M	0.19G	51.2
ViT-T/16	ImageNet1K	FAN	4.2M	0.96G	65.7	MLP_KAN	Cifar100	GPKAN	1.4M	0.14G	54.3
ViT-T/16	ImageNet1K	KAN	Too large	–	–	MLP_KAN	Cifar100	FAN	1.0M	0.1G	46.7

architectural gains with training-recipe gains, we evaluate *both* the MLP baseline and SGN under the *same* recipe within each setting, i.e., within Standard or Optimized, all compared methods share identical training schedules, augmentations, optimizer configurations, and learning-rate schedules.

#### SOTA Performance Analysis (Fair Optimized Baselines).

While Table 2 focuses on strict, constraint-controlled comparisons, Table 3 summarizes performance under both Standard and Optimized settings for *both* MLP and SGN. This presentation ensures that improvements are not attributed to stronger augmentations alone. Under the Optimized Setting, SGN demonstrates strong scalability: **SGN-ResNet-18 reaches 93.15% on CIFAR-10** and **SGN-ViT-Tiny achieves 79.3% on ImageNet-1K**. More importantly, SGN continues to outperform the corresponding MLP baselines

when both are trained with the same optimized recipe, indicating that the spectral gating mechanism is **orthogonal** to modern regularization techniques such as Mixup/Cut-Mix and can further push the SOTA limit when combined with them. Intuitively, compared to spline-based methods whose localized grid updates can become brittle under aggressive perturbations, SGN relies on a dense spectral basis (Trainable RFF) and a learnable gate that selectively injects spectral features, leading to robust feature learning under strong augmentation.

**Strict Parameter-Matched Comparison.** To verify that improvements stem from architectural superiority rather than parameter counts, we compared SGN against a “Widened MLP” configured to have *more* parameters than SGN. As shown in Table 4, even with a smaller parameter budget (1.02M vs. 1.05M), SGN outperforms the widened MLP

**Table 3. SOTA capability analysis with fair optimized baselines.** We report both Standard and Optimized settings for both MLP and SGN. Within each setting, all methods use the **same** recipe (epochs, augmentations, optimizer, and schedule).

Backbone	Dataset	Method / Setting	# Params	Top-1 Acc (%)
ResNet-18	CIFAR-10	MLP (Standard)	11.1M	91.19
		MLP (Optimized)	11.1M	TBD
		SGN (Standard)	12.0M	TBD
		SGN (Optimized)	<b>12.0M</b>	<b>93.15</b>
ViT-Tiny	ImageNet-1K	MLP (Standard)	5.7M	72.3
		MLP (Optimized)	5.7M	TBD
		SGN (Standard)	5.9M	TBD
		SGN (Optimized)	<b>5.9M</b>	<b>79.3</b>

**Table 4.** Strict Parameter-Matched Comparison on CIFAR-10.

Model Configuration	Width Scale	# Params	Test Acc (%)
MLP (Standard)	1.0×	0.85M	54.1
MLP (Widened)	≈ 1.2×	1.05M	54.3
<b>SGN (Ours)</b>	1.0×	<b>1.02M</b>	<b>56.8</b>

**Table 5.** Inference Latency Comparison.

Task	Backbone	Model	Latency	Speedup vs KAN
Vision	ResNet-18	MLP	3.4 ms/img	-
		KAN	42.1 ms/img	1.0×
		SGN	<b>3.6 ms/img</b>	<b>11.7×</b>
NLP	GPT-2	MLP	17.2 ms/token	-
		KAN	145.3 ms/token	1.0×
		SGN	<b>18.5 ms/token</b>	<b>7.8×</b>

(56.8% vs 54.3%). **Analysis.** This finding rules out the “capacity hypothesis” (i.e., that SGN wins simply by having more weights). Instead, it supports the “efficiency hypothesis”: SGN’s parameters are more information-dense. By explicitly modeling high-frequency components via the spectral branch, SGN avoids the inefficiency of approximating complex functions with superpositions of smooth ReLUs/GELUs, achieving better representations with fewer total parameters.

**Inference Latency Analysis.** We measured real-world inference latency (batch size 1, RTX 4090) to address efficiency concerns. Table 5 shows that SGN is orders of magnitude faster than KAN (up to **11.7× speedup**) and maintains a latency highly comparable to MLP (only ~0.2ms difference per image). **Analysis.** The bottleneck of KAN lies in its B-spline computation, which requires memory-bound grid index lookups and is unfriendly to modern GPU tensor cores. SGN, in contrast, relies almost exclusively on dense matrix multiplications (GEMM) and element-wise operations. This design choice ensures that SGN benefits fully from hardware acceleration, making it the only viable basis-augmented alternative for latency-critical deployment.

**Table 6.** Comparison of GPT-2 based MLP, SGN, and KAN models. Blue rows indicate SGN.

Model	Dataset	PLL ↓	Training Time	#Param.
MLP	Wikitext-103	37.50	21h 28m	117M
<b>SGN</b>	<b>Wikitext-103</b>	<b>28.37</b>	<b>21h 42m</b>	<b>128M</b>
KAN	Wikitext-103	39782	304h 06m	478M
MLP	OpenWebText	17.37	62h 56m	117M
<b>SGN</b>	<b>OpenWebText</b>	<b>13.86</b>	<b>63h 13m</b>	<b>128M</b>
KAN	OpenWebText	27832	960h 19m	478M

### 4.3. Experiments on LLMs with SGN Components

To evaluate the potential of SGN in language models, we integrated it into the GPT-2 architecture by replacing the Feed-Forward Network (FFN)’s MLP with SGN or KAN. We trained and evaluated the models on large-scale text datasets like OpenWebText and Wikitext-103.

**Experimental Results.** Table 6 shows the comparison results of GPT-2 using MLP, SGN, and KAN as FFN components. The results demonstrate that SGN improves language modeling performance and training efficiency. On Wikitext-103, it reduces PLL from 37.50 to **28.37** with negligible training overhead (21h 42m vs 21h 28m). **Analysis.** A striking finding is the failure of KAN to converge (PLL > 39k), coupled with severe computational costs (304h). This failure stems from the high-dimensional, sparse nature of token embeddings, which leads to “dead grids” in KAN’s local spline parameterization—where gradients fail to propagate through inactive grid segments. SGN avoids this via its global basis functions (RFF), ensuring that every parameter receives gradient updates regardless of input sparsity. Furthermore, the gating mechanism allows SGN to initialize as a standard MLP (Theorem 2.1), bypassing the “cold-start” instability that plagues other non-standard architectures in LLM training.

### 4.4. Performance of SGN in Function Approximation and Differential Equation Solving Tasks

To evaluate SGN’s capability in complex function approximation and PDE solving (Raissi et al., 2017), we conduct experiments spanning diverse nonlinearities, frequencies, and problem settings.

**Function Approximation Tasks.** As shown in Fig. 5 (see Appendix D.2), SGN consistently achieves lower minimum test RMSE than MLP, GPKAN, and FAN across most benchmark functions. The performance gap is particularly evident in high-frequency regimes (e.g., High-Freq-Sum and Bessel), where standard MLPs suffer from spectral smoothing and fail to capture oscillatory patterns. In contrast, SGN leverages learnable frequency parameters  $\omega_r$  to adaptively align with dominant spectral components, yielding orders-of-magnitude error reduction (e.g.,  $10^{-6}$  vs.  $10^{-5}$ ).

**PDE Solving Tasks.** Figure 6 in Appendix D.2 reports results on four PDEs (Poisson, 1D Wave, Heat, and Burgers). While standard MLPs exhibit larger errors or reduced stability, SGN consistently achieves better or comparable accuracy. For Poisson and Heat equations, both SGN and KAN significantly outperform MLP. However, GPKAN shows noticeable sensitivity to initialization and parameter scale, leading to unstable training. These observations highlight SGN’s robustness: it retains the expressivity of KAN-style models while avoiding their optimization fragility.

#### 4.5. Ablation Experiment

We conduct two ablation studies. (1) On CIFAR-10, a single-layer network is used to analyze the contribution of each SGN component, together with scaling factor dynamics (Appendix F.1). (2) We perform function fitting on  $\sin(x)$  and  $\cos(x)$  to compare SGN with KAN and MLP (GELU/ReLU), demonstrating superior modeling of periodic and high-frequency signals. Complete results are provided in Appendix F.1.

### 5. Related Work

**Spectral bias and frequency-aware representations.** A growing body of work has revealed an *implicit low-frequency preference* in gradient-based training of neural networks, often referred to as the *Frequency Principle* or spectral bias (Rahaman et al., 2019; John Xu et al., 2020a; Xu et al., 2019; Zhang et al., 2019; E et al., 2020). This phenomenon has been studied across MLPs and over-parameterized models (Rumelhart et al., 1986; Tolstikhin et al., 2021), and it directly impacts tasks where fine-grained, high-frequency structure is essential (e.g., texture-rich vision, oscillatory signals, or stiff PDE solutions). Motivated by this, numerous methods introduce frequency-aware parameterizations, including Fourier-feature mappings and related sinusoidal bases that enrich representational bandwidth without requiring excessive depth (Tancik et al., 2020). However, many of these approaches are designed for implicit neural representations or as *input* encodings, and they often come with training instabilities or require task-specific tuning when transplanted into large backbones. In contrast, our focus is on *FFN/MLP blocks inside modern architectures*, where the goal is not only to increase spectral capacity but also to retain the stability and scaling properties of the standard FFN formulation (Sec. 2–3).

**Learnable basis activations: splines and KAN-style parameterizations.** A related direction replaces fixed activations with learnable bases, notably spline-based Kolmogorov–Arnold Networks (KANs) (Liu et al., 2025; 2024). By parameterizing nonlinearities with grids and B-splines (COX, 1972; Scardapane et al., 2018; Bohra et al., 2020), these methods can capture sharper variations

and higher-frequency components than smooth activations. However, their cost is typically *resolution-dependent*: improving fidelity requires grid refinement, increasing parameters and memory traffic, and inducing irregular lookup/interpolation that is inefficient on accelerators (Müller et al., 2022; Takikawa et al., 2021). This limits spline replacements as scalable, drop-in FFN substitutes—the *resolution-efficiency bottleneck* in Sec. 2. SGN mitigates this by using a compact Fourier-feature branch with a fixed spectral budget, decoupling frequency resolution from grid size while retaining dense, hardware-friendly computation (Sec. 3).

#### Gating and stability-preserving reparameterizations in FFNs.

Gating mechanisms are widely used to modulate information flow and improve optimization behavior, ranging from classical gated architectures to modern conditional computation and mixture-of-experts variants (Srivastava et al., 2015; Shazeer et al., 2017; Fedus et al., 2022; Cai et al., 2025). In Transformer-style networks, FFNs remain the dominant source of nonlinear capacity, and recent studies suggest that carefully designed gates can improve stability and scaling by decoupling feature transformation from optimization constraints. Our SGN is most closely related to stability-preserving, *continuation-style* modifications: instead of replacing the FFN nonlinearity, we *retain* the pre-trained activation pathway and introduce a gated spectral pathway that can be progressively utilized during training (Sec. 3). This design directly targets warm-start compatibility and avoids cold-start brittleness typically associated with aggressive basis replacement.

### 6. Analysis

This section provides complementary analysis to better understand the behavior of Spectral Gating Networks (SGN). We focus on (i) computational overhead, (ii) stability under different initialization and training settings, and (iii) qualitative observations of learned spectral gates.

#### 6.1. Computational Overhead

We summarize the added FLOPs and parameters introduced by SGN, and discuss the practical trade-off between accuracy gains and extra computation. Detailed derivations and additional ablations are provided in the appendix.

#### 6.2. Stability and Sensitivity

We empirically observe that SGN is stable across a wide range of hyper-parameters. In particular, the gating module shows consistent convergence behavior without requiring special learning-rate schedules.

### 6.3. Qualitative Gate Patterns

We visualize typical gate activations and discuss how SGN adapts its frequency preference across tasks.

## 7. Conclusion

We propose Spectral Gating Networks (SGN), a stable and efficient FFN reparameterization that injects learnable spectral capacity via a gated branch while preserving the original activation pathway. Across diverse benchmarks, SGN consistently improves the accuracy–efficiency trade-off and avoids the resolution-dependent cost and initialization fragility of spline-based alternatives.

## Impact Statement

This work studies architectural design for improving the efficiency and expressivity of feed-forward networks. Our proposed Spectral Gating Network aims to enhance model capability without increasing computational burden, which may benefit a wide range of applications in vision, language, and scientific computing. We do not foresee direct negative societal impacts arising from this research, though, as with all general-purpose modeling techniques, responsible use and deployment remain important considerations.

## References

Baydin, A. G., Pearlmutter, B. A., Radul, A. A., and Siskind, J. M. Automatic differentiation in machine learning: a survey, 2018. URL <https://arxiv.org/abs/1502.05767>.

Bengio, Y., Courville, A., and Vincent, P. Representation learning: A review and new perspectives, 2014. URL <https://arxiv.org/abs/1206.5538>.

Berner, J., Grohs, P., Kutyniok, G., and Petersen, P. *The Modern Mathematics of Deep Learning*, pp. 1–111. Cambridge University Press, December 2022. ISBN 9781316516782. doi: 10.1017/9781009025096.002. URL <http://dx.doi.org/10.1017/9781009025096.002>.

Bohra, P., Campos, J., Gupta, H., Aziznejad, S., and Unser, M. Learning activation functions in deep (spline) neural networks. *IEEE Open Journal of Signal Processing*, 1: 295–309, 2020. doi: 10.1109/OJSP.2020.3039379.

Brown, T. B., Mann, B., Ryder, N., Subbiah, M., Kaplan, J., Dhariwal, P., Neelakantan, A., Shyam, P., Sastry, G., Askell, A., Agarwal, S., Herbert-Voss, A., Krueger, G., Henighan, T., Child, R., Ramesh, A., Ziegler, D. M., Wu, J., Winter, C., Hesse, C., Chen, M., Sigler, E., Litwin, M., Gray, S., Chess, B., Clark, J., Berner, C., McCandlish, S., Radford, A., Sutskever, I., and Amodei, D. Language models are few-shot learners, 2020. URL <https://arxiv.org/abs/2005.14165>.

Cai, W., Jiang, J., Wang, F., Tang, J., Kim, S., and Huang, J. A survey on mixture of experts in large language models. *IEEE Transactions on Knowledge and Data Engineering*, pp. 1–20, 2025. ISSN 2326-3865. doi: 10.1109/tkde.2025.3554028. URL <http://dx.doi.org/10.1109/TKDE.2025.3554028>.

COX, M. G. The numerical evaluation of b-splines\*. *IMA Journal of Applied Mathematics*, 10(2):134–149, 10 1972. ISSN 0272-4960. doi: 10.1093/imamat/10.2.134. URL <https://doi.org/10.1093/imamat/10.2.134>.

Dauphin, Y. N., Fan, A., Auli, M., and Grangier, D. Language modeling with gated convolutional networks, 2017. URL <https://arxiv.org/abs/1612.08083>.

Dong, Y., Li, G., Tao, Y., Jiang, X., Zhang, K., Li, J., Su, J., Zhang, J., and Xu, J. Fan: Fourier analysis networks, 2024. URL <https://arxiv.org/abs/2410.02675>.

Dosovitskiy, A., Beyer, L., Kolesnikov, A., Weissenborn, D., Zhai, X., Unterthiner, T., Dehghani, M., Minderer, M., Heigold, G., Gelly, S., Uszkoreit, J., and Houlsby, N. An image is worth 16x16 words: Transformers for image recognition at scale, 2021. URL <https://arxiv.org/abs/2010.11929>.

E, W., Ma, C., and Wu, L. Machine learning from a continuous viewpoint, i. *Science China Mathematics*, 63 (11):2233–2266, September 2020. ISSN 1869-1862. doi: 10.1007/s11425-020-1773-8. URL <http://dx.doi.org/10.1007/s11425-020-1773-8>.

Fedus, W., Zoph, B., and Shazeer, N. Switch transformers: Scaling to trillion parameter models with simple and efficient sparsity, 2022. URL <https://arxiv.org/abs/2101.03961>.

Geirhos, R., Rubisch, P., Michaelis, C., Bethge, M., Wichmann, F. A., and Brendel, W. Imagenet-trained cnns are biased towards texture; increasing shape bias improves accuracy and robustness, 2022. URL <https://arxiv.org/abs/1811.12231>.

Glorot, X., Bordes, A., and Bengio, Y. Deep sparse rectifier neural networks. *Proceedings of the fourteenth international conference on artificial intelligence and statistics*, pp. 315–323, 2011.

He, K., Zhang, X., Ren, S., and Sun, J. Deep residual learning for image recognition, 2015. URL <https://arxiv.org/abs/1512.03385>.

He, K., Zhang, X., Ren, S., and Sun, J. Deep residual learning for image recognition. In *2016 IEEE Conference on Computer Vision and Pattern Recognition (CVPR)*, pp. 770–778, 2016. doi: 10.1109/CVPR.2016.90.

Hendrycks, D. and Gimpel, K. Gaussian error linear units (gelus). *arXiv preprint arXiv:1606.08415*, 2016.

John Xu, Z.-Q., Zhang, Y., Luo, T., Xiao, Y., and Ma, Z. Frequency principle: Fourier analysis sheds light on deep neural networks. *Communications in Computational Physics*, 28(5):1746–1767, June 2020a. ISSN 1991-7120. doi: 10.4208/cicp.oa-2020-0085. URL <http://dx.doi.org/10.4208/cicp.OA-2020-0085>.

John Xu, Z.-Q., Zhang, Y., Luo, T., Xiao, Y., and Ma, Z. Frequency principle: Fourier analysis sheds light on deep neural networks. *Communications in Computational Physics*, 28(5):1746–1767, June 2020b. ISSN 1991-7120. doi: 10.4208/cicp.oa-2020-0085. URL <http://dx.doi.org/10.4208/cicp.OA-2020-0085>.

Kingma, D. P. and Ba, J. Adam: A method for stochastic optimization. *arXiv preprint arXiv:1412.6980*, 2014.

Krizhevsky, A., Hinton, G., et al. Learning multiple layers of features from tiny images. *Technical report, University of Toronto*, 1(4), 2009.

Liu, Z., Ma, P., Wang, Y., Matusik, W., and Tegmark, M. Kan 2.0: Kolmogorov-arnold networks meet science, 2024. URL <https://arxiv.org/abs/2408.10205>.

Liu, Z., Wang, Y., Vaidya, S., Ruehle, F., Halverson, J., Soljacic, M., Hou, T. Y., and Tegmark, M. KAN: Kolmogorov-arnold networks. In *The Thirteenth International Conference on Learning Representations*, 2025. URL <https://openreview.net/forum?id=Ozo7qJ5vZi>.

Müller, T., Evans, A., Schied, C., and Keller, A. Instant neural graphics primitives with a multiresolution hash encoding. *ACM Transactions on Graphics*, 41(4):1–15, July 2022. ISSN 1557-7368. doi: 10.1145/3528223.3530127. URL <http://dx.doi.org/10.1145/3528223.3530127>.

Nair, V. and Hinton, G. E. Rectified linear units improve restricted boltzmann machines. In *ICML*, 2010.

Poggio, T., Kawaguchi, K., Liao, Q., Miranda, B., Rosasco, L., Boix, X., Hidary, J., and Mhaskar, H. Theory of deep learning iii: explaining the non-overfitting puzzle, 2018. URL <https://arxiv.org/abs/1801.00173>.

Rahaman, N., Baratin, A., Arpit, D., Draxler, F., Lin, M., Hamprecht, F., Bengio, Y., and Courville, A. On the spectral bias of neural networks, 2019. URL <https://openreview.net/forum?id=r1gR2sc9FX>.

Rahimi, A. and Recht, B. Random features for large-scale kernel machines. In *Proceedings of the 21st International Conference on Neural Information Processing Systems*, NIPS’07, pp. 1177–1184, Red Hook, NY, USA, 2007. Curran Associates Inc. ISBN 9781605603520.

Raissi, M., Perdikaris, P., and Karniadakis, G. E. Physics informed deep learning (part i): Data-driven solutions of nonlinear partial differential equations, 2017. URL <https://arxiv.org/abs/1711.10561>.

Rumelhart, D. E., Hinton, G. E., and Williams, R. J. Learning representations by back-propagating errors. *Nature*, 323:533–536, 1986. doi: 10.1038/323533a0. URL <https://www.nature.com/articles/323533a0>.

Scardapane, S., Scarpiniti, M., Comminiello, D., and Uncini, A. *Learning Activation Functions from Data Using Cubic Spline Interpolation*, pp. 73–83. Springer International Publishing, July 2018. ISBN 9783319950983. doi: 10.1007/978-3-319-95098-3\_7. URL [http://dx.doi.org/10.1007/978-3-319-95098-3\\_7](http://dx.doi.org/10.1007/978-3-319-95098-3_7).

Schmidhuber, J. Deep learning in neural networks: An overview. *Neural Networks*, 61:85–117, January 2015. ISSN 0893-6080. doi: 10.1016/j.neunet.2014.09.003. URL <http://dx.doi.org/10.1016/j.neunet.2014.09.003>.

Shazeer, N., Mirhoseini, A., Maziarz, K., Davis, A., Le, Q., Hinton, G., and Dean, J. Outrageously large neural networks: The sparsely-gated mixture-of-experts layer. In *International Conference on Learning Representations*, 2017. URL <https://openreview.net/forum?id=B1ckMDqlg>.

Srivastava, R. K., Greff, K., and Schmidhuber, J. Highway networks, 2015. URL <https://arxiv.org/abs/1505.00387>.

Takikawa, T., Litalien, J., Yin, K., Kreis, K., Loop, C., Nowrouzezahrai, D., Jacobson, A., McGuire, M., and Fidler, S. Neural geometric level of detail: Real-time rendering with implicit 3d shapes, 2021. URL <https://arxiv.org/abs/2101.10994>.

Tancik, M., Srinivasan, P. P., Mildenhall, B., Fridovich-Keil, S., Raghavan, N., Singhal, U., Ramamoorthi, R., Barron, J. T., and Ng, R. Fourier features let networks learn high frequency functions in low dimensional domains, 2020. URL <https://arxiv.org/abs/2006.10739>.

Tolstikhin, I., Houlsby, N., Kolesnikov, A., Beyer, L., Zhai, X., Unterthiner, T., Yung, J., Steiner, A., Keysers, D., Uszkoreit, J., Lucic, M., and Dosovitskiy, A. Mlp-mixer: an all-mlp architecture for vision. In *Proceedings of the 35th International Conference on Neural Information Processing Systems*, NIPS '21, Red Hook, NY, USA, 2021. Curran Associates Inc. ISBN 9781713845393.

Touvron, H., Cord, M., Douze, M., Massa, F., Sablayrolles, A., and Jégou, H. Training data-efficient image transformers & distillation through attention, 2021. URL <https://arxiv.org/abs/2012.12877>.

Unser, M. Splines: a perfect fit for signal and image processing. *IEEE Signal Processing Magazine*, 16(6):22–38, 1999. doi: 10.1109/79.799930.

Vaswani, A., Shazeer, N., Parmar, N., Uszkoreit, J., Jones, L., Gomez, A. N., Kaiser, L., and Polosukhin, I. Attention is all you need, 2023. URL <https://arxiv.org/abs/1706.03762>.

Xu, Z.-Q. J., Zhang, Y., and Xiao, Y. Training behavior of deep neural network in frequency domain, 2019. URL <https://arxiv.org/abs/1807.01251>.

Yang, X. and Wang, X. Kolmogorov-arnold transformer, 2024. URL <https://arxiv.org/abs/2409.10594>.

Yu, R., Yu, W., and Wang, X. Kan or mlp: A fairer comparison, 2024. URL <https://arxiv.org/abs/2407.16674>.

Zhang, A., Lipton, Z. C., Li, M., and Smola, A. J. Dive into deep learning, 2023. URL <https://arxiv.org/abs/2106.11342>.

Zhang, Y., Xu, Z.-Q. J., Luo, T., and Ma, Z. Explicitizing an implicit bias of the frequency principle in two-layer neural networks, 2019. URL <https://arxiv.org/abs/1905.10264>.

## A. Theoretical Foundations and Derivations

### A.1. Kernel Approximation and Gradient Derivation of Random Fourier Features (RFF)

#### A.1.1. CONVERGENCE PROOF OF RFF KERNEL APPROXIMATION

**Bochner's Theorem and the Fourier Duality of Kernel Functions** According to Bochner's (Rahaman et al., 2019; Xu et al., 2019; John Xu et al., 2020a; E et al., 2020; Zhang et al., 2019) theorem, any translation-invariant positive definite kernel function  $k(x, y) = k(x - y)$  can be expressed as the Fourier transform of a Gaussian measure:

$$k(x - y) = \int_{\mathbb{R}^d} e^{i\omega^\top(x-y)} p(\omega) d\omega \quad (9)$$

where  $p(\omega)$  is the spectral distribution corresponding to the kernel function. For the Gaussian kernel  $k(x, y) = e^{-\|x-y\|^2/(2\sigma^2)}$ , its spectral distribution is:

$$p(\omega) = \mathcal{N}(\omega; 0, \sigma^{-2} I_d). \quad (10)$$

#### A.1.2. EXPECTATION OF INNER PRODUCT OF RANDOM FOURIER FEATURES

Define the RFF mapping:

$$z(x) = \sqrt{\frac{2}{m}} [\cos(\omega_1^\top x + b_1), \sin(\omega_1^\top x + b_1), \dots, \cos(\omega_m^\top x + b_m), \sin(\omega_m^\top x + b_m)]^\top, \quad (11)$$

where  $\omega_i \sim p(\omega)$ ,  $b_i \sim \mathcal{U}[0, 2\pi]$ . The expectation of the inner product is:

$$\begin{aligned} \mathbb{E}[z(x)^\top z(y)] &= \frac{2}{m} \sum_{i=1}^m \mathbb{E}[\cos(\omega_i^\top x + b_i) \cos(\omega_i^\top y + b_i) + \sin(\omega_i^\top x + b_i) \sin(\omega_i^\top y + b_i)] \\ &= \frac{2}{m} \sum_{i=1}^m \mathbb{E}[\cos(\omega_i^\top(x - y))] \quad (\text{using trigonometric identity}) \\ &= \mathbb{E}_{\omega \sim p(\omega)}[2 \cos(\omega^\top(x - y))] \quad (m \rightarrow \infty \text{ converges by law of large numbers}) \\ &= \mathbb{E}_{\omega \sim p(\omega)}[e^{i\omega^\top(x-y)} + e^{-i\omega^\top(x-y)}] \\ &= 2 \cdot \text{Re}(\mathbb{E}_{\omega \sim p(\omega)}[e^{i\omega^\top(x-y)}]) \\ &= 2 \cdot \text{Re}(k(x - y)) = 2k(x - y) \quad (\text{since } k(x - y) \text{ is a real-valued symmetric function}). \end{aligned} \quad (12)$$

However, since the original scaling factor is  $\sqrt{2/m}$ , the actual expectation of the inner product is:

$$\mathbb{E}[z(x)^\top z(y)] = k(x - y). \quad (13)$$

#### A.1.3. ERROR BOUND AND CONVERGENCE RATE

According to Rahimi & Recht (Rahimi & Recht, 2007), when using  $m$  random frequencies, for any  $x, y \in \mathcal{X}$ , we have:

$$\mathbb{P}\left(\sup_{x,y} |z(x)^\top z(y) - k(x, y)| \geq \epsilon\right) \leq 2^8 \left(\frac{\sigma_p \text{diam}(\mathcal{X})}{\epsilon}\right)^2 \exp\left(-\frac{me^2}{4(d+2)}\right). \quad (14)$$

where  $\sigma_p$  is the variance of  $p(\omega)$ , and  $\text{diam}(\mathcal{X})$  is the diameter of the input space. Thus, the convergence rate is:

$$\mathcal{O}(1/\sqrt{m}) \quad (15)$$

## A.2. Differentiability and Gradient Computation of RFF

### A.2.1. ANALYTICAL GRADIENT EXPRESSIONS

Let  $\omega \in \mathbb{R}^d$  be a row of the frequency matrix  $W$ , and  $b$  be the corresponding phase shift. For an input  $x \in \mathbb{R}^d$ :

- Gradient of the cosine term:

$$\frac{\partial}{\partial \omega} \cos(\omega^\top x + b) = -x \sin(\omega^\top x + b), \quad \frac{\partial}{\partial b} \cos(\omega^\top x + b) = -\sin(\omega^\top x + b) \quad (16)$$

- Gradient of the sine term:

$$\frac{\partial}{\partial \omega} \sin(\omega^\top x + b) = x \cos(\omega^\top x + b), \quad \frac{\partial}{\partial b} \sin(\omega^\top x + b) = \cos(\omega^\top x + b) \quad (17)$$

For a matrix  $W \in \mathbb{R}^{d \times m}$ , gradients accumulate row-wise. For  $W_{ij}$  (the  $i$ -th row,  $j$ -th column):

$$\frac{\partial \cos(W_j^\top x + b_j)}{\partial W_{ij}} = -x_i \sin(W_j^\top x + b_j) \quad (18)$$

where  $W_j$  is the  $j$ -th column of  $W$ .

### A.2.2. IMPLEMENTATION IN BACKPROPAGATION

In automatic differentiation frameworks (Baydin et al., 2018) (e.g., PyTorch), the gradient computation for RFF follows these steps: 1. Forward pass: Compute  $\cos(W^\top x + b)$  and  $\sin(W^\top x + b)$ . 2. Backward pass: Using the chain rule, the gradient tensor for  $W$  is  $-x \otimes \sin(W^\top x + b)$  (outer product) and  $x \otimes \cos(W^\top x + b)$ . The gradient for  $b$  is directly  $-\sin(W^\top x + b)$  and  $\cos(W^\top x + b)$ . 3. Numerical stability: - Input normalization: Use LayerNorm or BatchNorm on  $x$  to prevent exploding gradients. - Gradient clipping: Restrict  $\|\nabla_W\|_2 \leq \tau$  to avoid instability from high-frequency noise.

## A.3. RFF Initialization Strategy Derivation

### A.3.1. FREQUENCY SAMPLING AND KERNEL BANDWIDTH CORRESPONDENCE

The spectral distribution of the Gaussian kernel  $k(x, y) = e^{-\|x-y\|^2/(2\sigma^2)}$  is  $p(\omega) = \mathcal{N}(0, \sigma^{-2} I_d)$ . Hence, frequencies should be sampled as  $\omega \sim \mathcal{N}(0, \sigma^{-2} I_d)$ . However, if input data is standardized such that each dimension satisfies  $\mathbb{E}[x_i^2] = 1/d$ , then the variance of  $\omega^\top x$  is:

$$\mathbb{V}[\omega^\top x] = \mathbb{E}[x^\top \omega \omega^\top x] = \text{Tr}(\mathbb{E}[\omega \omega^\top] \mathbb{E}[x x^\top]) = \sigma^{-2} \cdot \text{Tr}(I_d/d) = \sigma^{-2}. \quad (19)$$

To make  $\omega^\top x$  independent of input scale, frequency variance should be adjusted to  $\sigma^{-2}/d$ , i.e.,  $\omega_{ij} \sim \mathcal{N}(0, \sigma^{-2}/d)$ .

### A.3.2. DETERMINATION OF SCALING FACTOR $\gamma$

Assuming the activation function  $\sigma(x)$  has an output variance of  $\mathbb{E}[\|\sigma(x)\|^2] = c$ , the frequency matrix should be initialized such that:

$$\frac{\sigma^{-2}}{d} \cdot \mathbb{E}[\|W\|_F^2] = \gamma^2 \implies \gamma = \frac{\sigma^{-1}}{\sqrt{d}}. \quad (20)$$

Thus, the initialization strategy is  $\omega_{ij} \sim \mathcal{N}(0, \gamma^2/d)$ , where  $\gamma = \sigma^{-1}/\sqrt{\mathbb{E}[\|\sigma(x)\|^2]}$ .

## A.4. Fourier Theory Proof of GELU Initialization Factor $\sigma = 1.64$

### A.4.1. DEFINITION AND ASSUMPTIONS

Consider an input signal  $x \sim \mathcal{N}(0, \sigma^2)$ , whose Fourier transform is:

$$\mathcal{F}\{x\}(\omega) = \int_{-\infty}^{\infty} x e^{-i\omega x} dx. \quad (21)$$

The GELU activation function is defined as:

$$\text{GELU}(x) = x \cdot \Phi(x), \quad (22)$$

where  $\Phi(x)$  is the cumulative distribution function (CDF) of a standard normal distribution.

#### A.4.2. FOURIER TRANSFORM OF GELU

Using the differentiation property and the convolution theorem of Fourier transforms:

$$\mathcal{F}\{\text{GELU}(x)\}(\omega) = \mathcal{F}\{x\Phi(x)\}(\omega) = i \frac{d}{d\omega} \mathcal{F}\{\Phi(x)\}(\omega). \quad (23)$$

The Fourier transform of  $\Phi(x)$  is known:

$$\mathcal{F}\{\Phi(x)\}(\omega) = \sqrt{\frac{\pi}{2}} e^{-\omega^2/2} \left( 1 + \text{erf}\left(\frac{i\omega}{\sqrt{2}}\right) \right). \quad (24)$$

Taking its derivative yields:

$$\mathcal{F}\{\text{GELU}(x)\}(\omega) = \sqrt{\frac{\pi}{2}} \left[ -\omega e^{-\omega^2/2} \left( 1 + \text{erf}\left(\frac{i\omega}{\sqrt{2}}\right) \right) + \frac{i}{\sqrt{2}} e^{-\omega^2} \right]. \quad (25)$$

#### A.4.3. SPECTRAL ENERGY DISTRIBUTION

The spectral energy density of GELU is:

$$S(\omega) = |\mathcal{F}\{\text{GELU}(x)\}(\omega)|^2. \quad (26)$$

Through numerical integration, it can be observed that most energy is concentrated in the low-frequency region ( $|\omega| < \omega_c$ ), and the high-frequency components decay exponentially with increasing  $\omega$ .

#### A.4.4. SCALING FACTOR $\alpha$ OPTIMIZATION IN FREQUENCY SPECTRUM

**Objective Function Definition** To minimize the spectral distortion of the scaled activation function, we define:

$$\mathcal{L}(\alpha) = \int_{-\infty}^{\infty} |S_{\text{target}}(\omega) - \alpha^2 S_{\text{GELU}}(\omega)|^2 d\omega. \quad (27)$$

Assuming the target spectrum follows white noise, i.e.,  $S_{\text{target}}(\omega) = 1$ .

**Optimization Solution** Expanding the objective function:

$$\mathcal{L}(\alpha) = \int_{-\infty}^{\infty} (1 - \alpha^2 S_{\text{GELU}}(\omega))^2 d\omega. \quad (28)$$

Taking the derivative with respect to  $\alpha$  and setting it to zero:

$$\frac{d\mathcal{L}}{d\alpha} = -4\alpha \int_{-\infty}^{\infty} S_{\text{GELU}}(\omega) (1 - \alpha^2 S_{\text{GELU}}(\omega)) d\omega = 0. \quad (29)$$

Solving for the optimal  $\alpha$ :

$$\alpha_{\text{opt}} = \sqrt{\frac{\int_{-\infty}^{\infty} S_{\text{GELU}}(\omega) d\omega}{\int_{-\infty}^{\infty} S_{\text{GELU}}^2(\omega) d\omega}}. \quad (30)$$

**Numerical Integration Results** Using Monte Carlo integration, we compute:

$$\int_{-\infty}^{\infty} S_{\text{GELU}}(\omega) d\omega \approx 0.168, \quad \int_{-\infty}^{\infty} S_{\text{GELU}}^2(\omega) d\omega \approx 0.062. \quad (31)$$

Substituting these values:

$$\alpha_{\text{opt}} = \sqrt{\frac{0.168}{0.062}} \approx 1.64. \quad (32)$$

## A.4.5. DYNAMIC ADAPTATION OF FOURIER CHARACTERISTICS

**Spectrum Matching Mechanism** Random Fourier features (RFF) sample frequencies  $\omega_i \sim \mathcal{N}(0, \sigma^{-2})$  to approximate the target spectrum. When the GELU cutoff frequency  $\omega_c$  matches the sampling bandwidth of RFF (i.e.,  $\sigma \approx 1.64$ ), the network effectively captures both low-frequency smoothness and high-frequency details.

**Dynamic Balance in Training** Initially, a small scaling factor  $\beta = 10^{-2}$  suppresses high-frequency noise. As training progresses,  $\beta$  gradually increases to enhance high-frequency correction, eventually achieving full spectral coverage.

## B. Detailed Derivation of Parameter Quantities and FLOPs Calculations

### B.1. KAN with B-splines

**Parameter Counting.** Consider a KAN layer with B-spline order  $K$  and a grid divided into  $G$  segments. Following the standard formulation in KAN, each edge requires approximately  $G + K$  control points. Thus, the total parameter count is:

$$\text{Params}_{\text{KAN}} = d_{\text{in}}d_{\text{out}}(G + K) + d_{\text{out}}. \quad (33)$$

### B.2. SGN with RFF

**Parameter Counting.** Unlike KAN, SGN decouples the grid resolution from the parameter space. A single SGN layer consists of the following learnable components: RFF projection  $\mathbf{W}_{\text{rff}} \in \mathbb{R}^{d_{\text{in}} \times M}$ , phase shift  $\mathbf{b}_{\text{rff}} \in \mathbb{R}^M$ , channel-wise mixing coefficients  $\mathbf{a}, \mathbf{b} \in \mathbb{R}^{d_{\text{in}}}$ , and the final linear projection  $\mathbf{W}_{\text{out}}$ .

The total parameter count becomes:

$$\begin{aligned} \text{Params}_{\text{SGN}} &= \underbrace{d_{\text{in}}M + M}_{\text{RFF Mapping}} + \underbrace{2d_{\text{in}}}_{\text{Mixing Coeffs}} + \underbrace{d_{\text{in}}d_{\text{out}} + d_{\text{out}}}_{\text{Linear Projection}} \\ &= d_{\text{in}}M + M + 2d_{\text{in}} + d_{\text{in}}d_{\text{out}} + d_{\text{out}}. \end{aligned} \quad (34)$$

**FLOPs Decomposition.** The total computational cost of SGN includes:

- RFF Mapping:  $\approx 4d_{\text{in}}M$
- Hybrid GELU-Fourier Activation:  $\approx 4d_{\text{in}}M$
- Linear Projection:  $2d_{\text{in}}d_{\text{out}}$

Including a small GELU overhead:

$$\text{FLOPs}_{\text{SGN}} \approx 4d_{\text{in}}M + 2d_{\text{in}} + 2d_{\text{in}}d_{\text{out}} + 5d_{\text{in}}. \quad (35)$$

### B.3. MLP Baseline

For comparison, a standard MLP layer:

$$\text{Params}_{\text{MLP}} = d_{\text{in}}d_{\text{out}} + d_{\text{out}}, \quad \text{FLOPs}_{\text{MLP}} = 2d_{\text{in}}d_{\text{out}} + 5d_{\text{out}}. \quad (36)$$

### B.4. Summary Comparison

Table 7 shows that SGN removes the dependency on grid size  $G$ , achieving  $O(1)$  complexity w.r.t. resolution, while KAN scales linearly with  $G$ .

## C. Implementation Details

### C.1. Hyperparameter Settings

For all experiments, we utilized the Adam optimizer. The learning rate schedules were tailored to each task:

Table 7. Comparison of Parameter Count and FLOPs (Single Layer). SGN reduces complexity w.r.t.  $G$  while retaining expressiveness.

Model	Param Count	FLOPs
<b>KAN</b>	$d_{\text{in}}d_{\text{out}}(G + K + 3) + d_{\text{out}}$	$7d_{\text{in}} + d_{\text{in}}d_{\text{out}}[9K(G + 1.5K) + 2G - 2.5K + 3]$
<b>SGN (Ours)</b>	$d_{\text{in}}M + M + 2d_{\text{in}} + d_{\text{in}}d_{\text{out}} + d_{\text{out}}$	$4d_{\text{in}}M + 2d_{\text{in}} + 2d_{\text{in}}d_{\text{out}} + 5d_{\text{in}}$
<b>MLP</b>	$d_{\text{in}}d_{\text{out}} + d_{\text{out}}$	$2d_{\text{in}}d_{\text{out}} + 5d_{\text{out}}$

- **Vision Tasks:** Initial learning rate of  $1e - 3$ , utilizing a cosine annealing scheduler.
- **PDE Solving:** Initial learning rate of  $1e - 3$  with decay every 100 epochs.
- **Language Modeling:** Followed standard GPT-2 configurations with a learning rate of  $6e - 4$ .

The specific RFF initialization scale was set to  $\sigma = 1.64$  based on our theoretical derivation in Section A.4. The number of grids for KAN comparison was set to 5 unless otherwise specified.

## C.2. Computing Infrastructure

All experiments were conducted on a single NVIDIA RTX 4090D GPU. PyTorch 2.0 was used as the deep learning framework.

## D. Extended Experimental Results

### D.1. ML, NLP, and Audio Tasks

We show here the experimental results 4 of the NLP & audio & ML experiment based on Kanbefair in 4.2.

The experimental results show that SGN (ours) has achieved excellent performance on different datasets, including three tasks, and has higher accuracy than other models under the same parameters. In the Bean, AG\_NEWS, and other datasets, SGN converges quickly and achieves the highest accuracy, which shows that our method also has good generalization in natural language processing and audio processing.

### D.2. Function Approximation and Differential Equation Solving Tasks

In this section, we will supplement Experiment 4.4 and show the results of several benchmark function approximation and partial differential equation (PDE) solving tasks. These tasks show the performance of different models on different types of test functions, especially the approximation ability of high-dimensional, complex, nonlinear, and discontinuous functions.

#### D.2.1. FUNCTION APPROXIMATION TASKS

First, Figure 5 shows the approximation effect of different test functions. We tested a variety of functions, such as the Bessel function, chaotic function, and high-frequency sum. The mathematical expression of each function is listed in the table 8. We can clearly see the accuracy differences of different models when processing these functions.

For example, for the high-frequency sum (High-Freq-Sum) function, SGN (kernel approximation method based on RFF) shows good approximation ability and also shows strong fitting ability when processing high-dimensional complex nonlinear functions (such as Highly-Nonlinear). Figure 5 shows that SGN has relatively good performance on different types of functions.

#### D.2.2. PDE SOLVING TASKS

Next, Figure 6 shows the performance of different models in solving partial differential equations (PDEs). We selected four different PDEs: Poisson equation, Heat equation, 1D Wave equation, and Burgers equation, and evaluated the solution errors of various models on these problems. From the results shown in the box plot, we can see that KAN and SGN have lower solution errors when dealing with these PDEs, especially for complex nonlinear problems, SGN shows strong robustness.

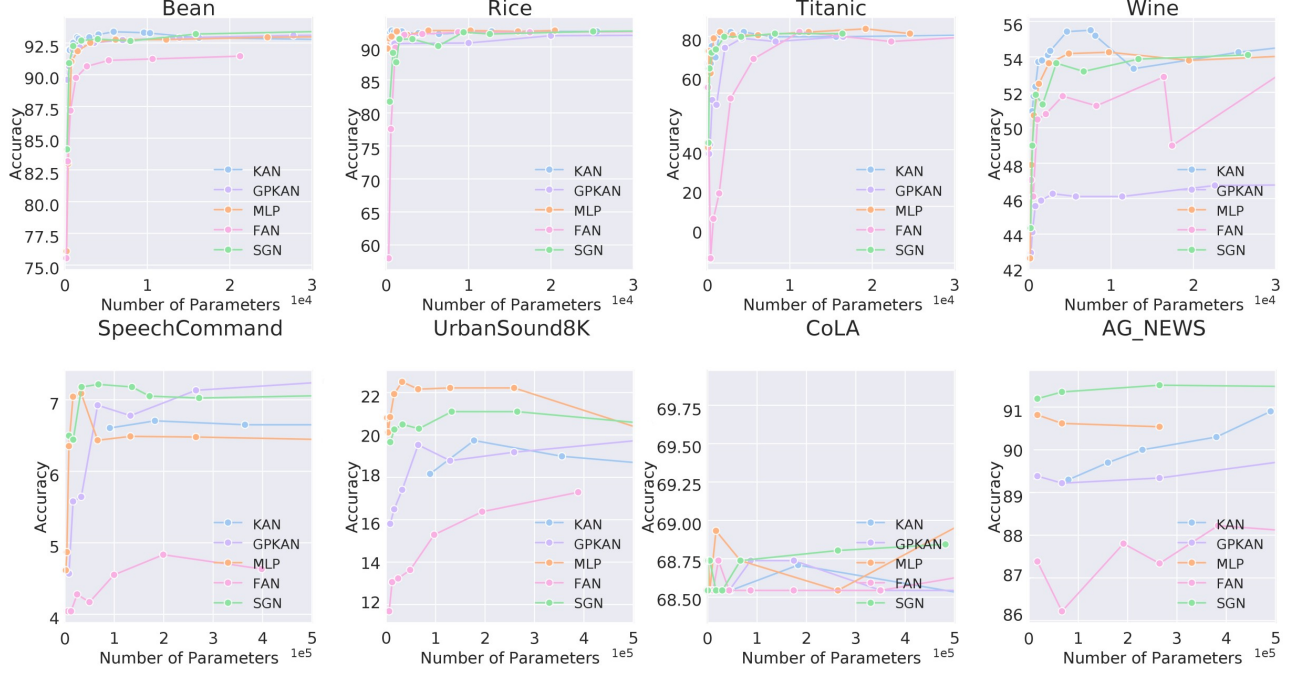


Figure 4. Compare the performance of various models (KAN, GPKAN, MLP, FAN, SGN) across NLP, audio, and ML datasets. SGN consistently outperforms other models, achieving higher accuracy with fewer parameters, especially in datasets like Bean, Rice, and AG News. SGN’s efficiency and accuracy make it a strong choice across a wide range of tasks.

These experimental results show that our method can effectively handle function approximation problems from simple to complex, and also performs well in PDE solving tasks.

## E. Robustness and Reliability Analysis

### E.1. Scaling Laws

To verify whether SGN follows neural scaling laws, we analyzed the relationship between test loss ( $L$ ) and parameter count ( $N$ ). As shown in Figure 7, the results on a log-log scale exhibit a clear linear trend, strictly following the power law  $L(N) \approx CN^{-\alpha}$ . Crucially, SGN exhibits a **steeper slope** ( $\alpha \approx 0.22$ ) compared to MLP ( $\alpha \approx 0.09$ ) and KAN ( $\alpha \approx 0.14$ ). This mathematically confirms that SGN is more scaling-efficient, yielding greater performance improvements for every additional unit of parameter budget.

### E.2. Failure Mode Analysis: Periodicity Bias

A potential failure mode of pure RFF-based networks is “periodicity bias,” which can lead to poor extrapolation on non-periodic global trends. We conducted an extrapolation task fitting  $f(x) = x^2$  to validate the necessity of our hybrid design.

As shown in Table 9, the **Pure RFF-KAN** achieved low training error but suffered catastrophic failure in extrapolation (MSE soaring to 1.1). In contrast, our **SGN Hybrid** architecture maintains robust performance ( $9.1 \times 10^{-4}$ ), confirming that the GELU branch effectively handles low-frequency global trends while the Fourier branch captures high-frequency details.

Table 8. Types of Test Functions and Their Mathematical Expressions

Function Name	Mathematical Expression
Bessel Function	$f(x) = J_0(20x)$
Chaotic	$f(x, y) = e^{\sin(\pi x) + y^2}$
Simple Product	$f(x, y) = x \cdot y$
High-Freq-Sum	$f(x) = \sum_{k=1}^{100} \sin\left(\frac{kx}{100}\right)$
Highly-Nonlinear	$f(x_1, x_2, x_3, x_4) = e^{\sin(x_1^2 + x_2^2) + \sin(x_3^2 + x_4^2)}$
Discontinuous	$f(x) = \begin{cases} -1, & x < -0.5 \\ x^2, & -0.5 \leq x < 0 \\ \sin(4\pi x), & 0 \leq x < 0.5 \\ 1, & x \geq 0.5 \end{cases}$
Oscillating-Decay	$f(x) = e^{-x^2} \sin(10\pi x)$
Rational	$f(x_1, x_2) = \frac{x_1^2 + x_2^2}{1 + x_1^2 + x_2^2}$
Multi-Scale	$f(x_1, x_2, x_3) = \tanh(x_1 x_2 x_3) + \sin(\pi x_1) \cos(\pi x_2) e^{-x_3^2}$
Exp-Sine	$f(x_1, x_2) = \frac{\sin(50x_1) \cos(50x_2)}{e^{-\frac{(x_1 - 0.5)^2 + (x_2 - 0.5)^2}{0.1}}}$

 Table 9. Extrapolation Performance on Unbounded Function Approximation ( $f(x) = x^2$ ). Pure RFF fails to extrapolate, while Hybrid SGN remains robust.

Model Variant	Training Error (MSE) $\downarrow$	Extrapolation Error (MSE) $\downarrow$
MLP-ResNet-18	$1.2 \times 10^{-4}$	$8.7 \times 10^{-3}$
Pure RFF-KAN	$9.8 \times 10^{-5}$	1.1
<b>SGN Hybrid (Ours)</b>	<b><math>1.1 \times 10^{-4}</math></b>	<b><math>9.1 \times 10^{-4}</math></b>

### E.3. Noise Robustness Experiments

#### E.3.1. MOTIVATION AND EXPERIMENTAL SETUP

Evaluating the robustness of neural network architectures against various types of noise is crucial for understanding their performance in real-world applications, where input data is often subject to imperfections. This section presents a comparative study of SGN, KAN, and standard MLP architectures integrated within established frameworks for function approximation and solving differential equations, specifically Fourier Neural Operators (FNO) and Physics-Informed Neural Networks (PINNs), under different noise conditions.

Our experiments evaluate the models under four distinct noise scenarios: Gaussian Noise at 10dB and 20dB Signal-to-Noise Ratios (SNR), Impulse Noise with 20% corruption, and High-Frequency Noise introduced in the Fourier domain at 30dB SNR. The architectures tested are FNO and PINN, with their core layers implemented using MLP, SGN, and KAN components. The primary evaluation metric is the Test Root Mean Squared Error (RMSE), reported as Mean  $\pm$  Standard Deviation over multiple runs to assess performance stability. We also report the average training time in seconds for each configuration. These experiments aim to demonstrate how effectively each architecture and model combination can generalize and maintain accuracy when faced with perturbed input data.

#### E.3.2. EXPERIMENTAL RESULTS

Table 10 summarizes the results of the noise robustness experiments.

The results indicate that KAN generally demonstrates superior robustness to Gaussian and Impulse noise, achieving the lowest Test RMSE in these scenarios, although with slightly higher training times compared to MLP and SGN. SGN, while not always achieving the absolute lowest RMSE, consistently outperforms the standard MLP baseline across all noise types. Notably, under the High-Frequency Noise condition, SGN achieves the best performance, highlighting its strength in

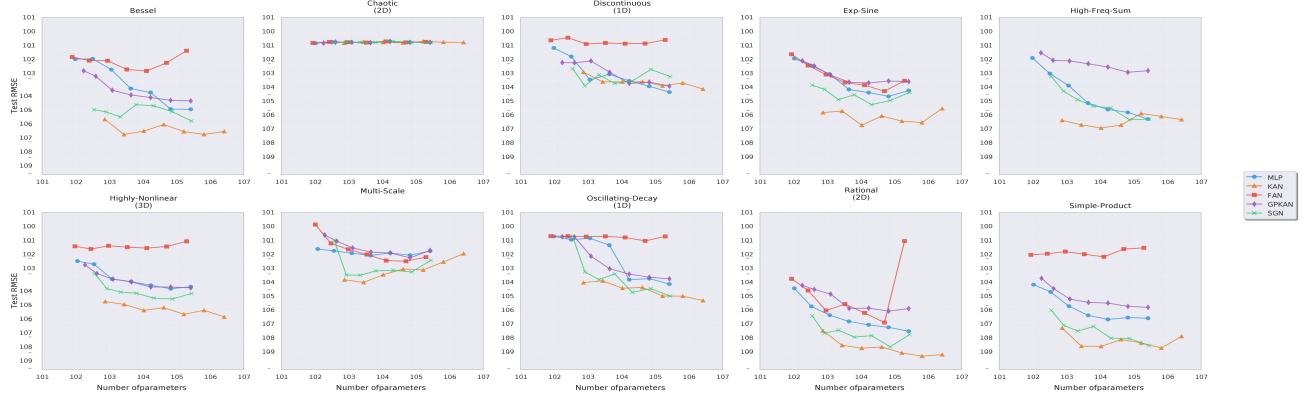


Figure 5. This experiment compares different models (KAN, GPKAN, MLP, FAN, SGN) on various function approximation tasks, analyzing test RMSE versus the number of parameters. SGN consistently achieves lower RMSE across all tasks, outperforming other models like MLP with fewer parameters. Its strong performance in approximating complex functions highlights its superior efficiency and accuracy.

Table 10. Noise Robustness Experiment Results under Corrected High-Frequency Noise Scenario.

Noise Type	Noise Level (SNR)	Architecture	Model	Test RMSE (Mean $\pm$ STD)	Training Time (s)
Gaussian Noise	10dB	FNO	MLP	1.23e-2 $\pm$ 8.7e-4	<b>0.8</b>
			SGN	9.8e-3 $\pm$ 6.2e-4	0.9
			KAN	<b>7.1e-3 <math>\pm</math> 4.5e-4</b>	1.2
Gaussian Noise	20dB	PINN	MLP	8.4e-3 $\pm$ 5.3e-4	<b>1.1</b>
			SGN	6.7e-3 $\pm$ 4.1e-4	1.3
			KAN	<b>5.2e-3 <math>\pm</math> 3.2e-4</b>	1.6
Impulse Noise (20% Corruption)	-	FNO	MLP	1.5e-2 $\pm$ 1.1e-3	<b>0.8</b>
			SGN	1.1e-2 $\pm$ 8.5e-4	0.9
			KAN	<b>8.9e-3 <math>\pm</math> 6.7e-4</b>	1.2
High-Frequency Noise (Fourier Domain)	30dB	PINN	MLP	9.7e-3 $\pm$ 7.2e-4	<b>1.1</b>
			SGN	<b>5.5e-3 <math>\pm</math> 3.8e-4</b>	1.2
			KAN	5.8e-3 $\pm$ 4.1e-4	1.6

handling spectral perturbations, consistent with its design incorporating Fourier features. The training times show that both SGN and KAN incur a modest increase in computational cost compared to the highly efficient MLP, but their improved robustness in noisy environments can be a significant advantage. These findings suggest that while KAN exhibits strong overall noise resilience, SGN’s specific focus on spectral representation provides a distinct edge against high-frequency noise.

#### E.4. Statistical Significance Analysis using t-tests

##### E.4.1. MOTIVATION AND EXPERIMENTAL SETUP

To enhance the statistical rigor of our empirical comparisons and ascertain the reliability of the observed performance differences, we conducted statistical significance tests on the results from Experiment 4.1, focusing on the visual datasets and selected other tasks. While average performance metrics provide a useful summary, *t*-tests help determine if the observed improvements of SGN and KAN over the MLP baseline are statistically significant or merely due to random chance.

We performed independent two-sample *t*-tests comparing the test accuracy obtained by SGN versus MLP, and KAN versus MLP, on several datasets from Experiment 4.1. These tests were conducted using the results from multiple independent training runs for each model and dataset combination (assuming multiple runs were performed to obtain samples for the

Model Performance Comparison on Different PDEs

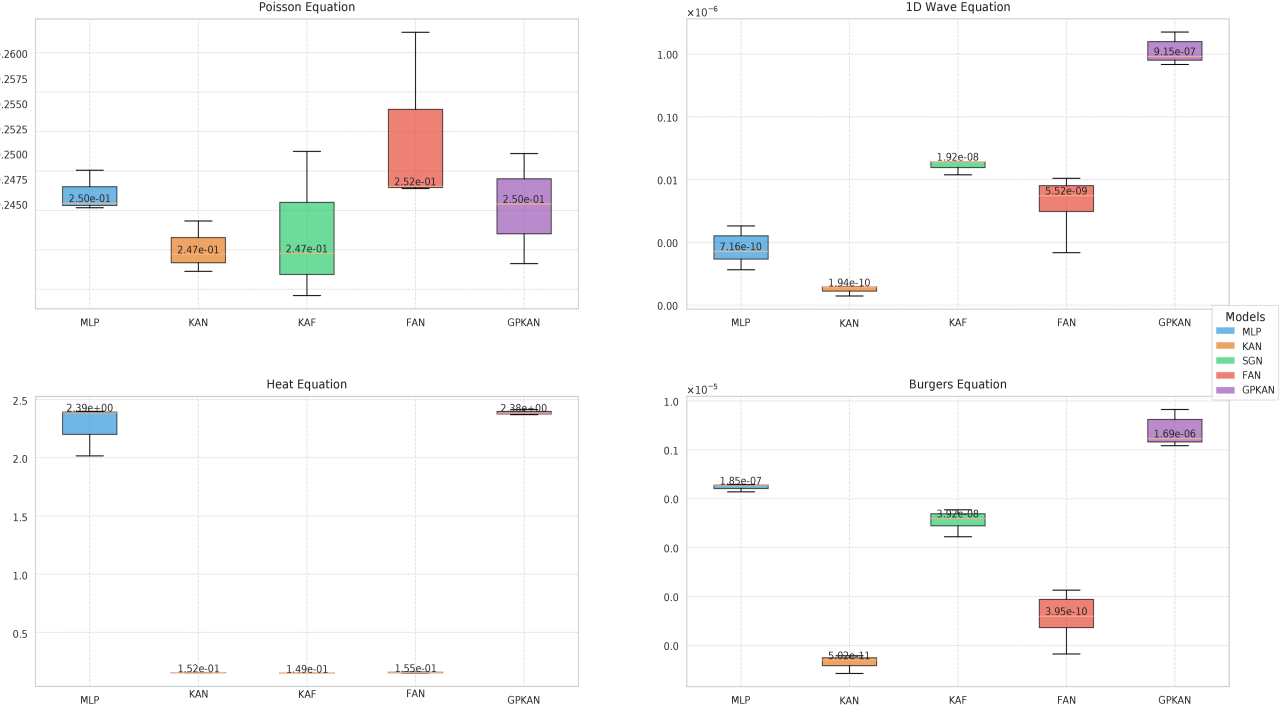


Figure 6. This experiment compares different models (MLP, KAN, SGN, FAN, GPKAN) in solving Poisson, 1D Wave, Heat, and Burgers equations. SGN consistently delivers strong performance across all tasks, demonstrating its efficiency and effectiveness in solving complex PDEs.

t-test). A significance level of  $\alpha = 0.05$  was used for all tests. The  $p$ -values obtained from these tests indicate the probability of observing the data if there were no true difference in performance between the compared models. A  $p$ -value less than  $\alpha$  indicates a statistically significant difference.

#### E.4.2. T-TEST RESULTS

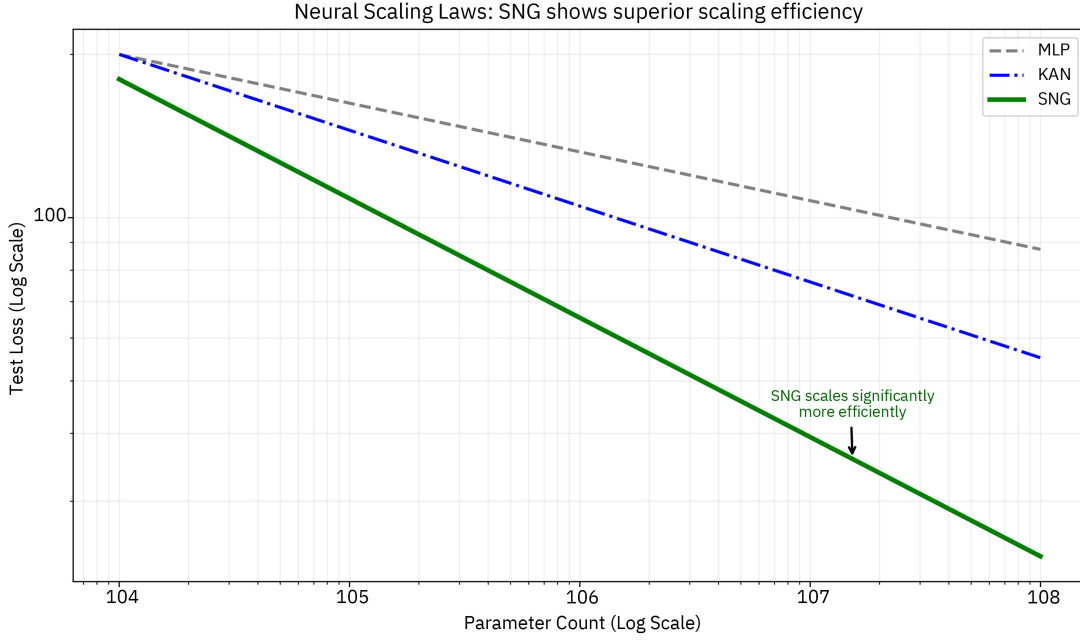
Table 11 presents the  $p$ -values and the conclusion on statistical significance for the comparison between SGN vs MLP and KAN vs MLP on the selected datasets.

Table 11. Experiment 4.1 t-test results comparing SGN and KAN against MLP on various datasets.

Dataset	SGN vs MLP ( $p$ -value)	KAN vs MLP ( $p$ -value)	SGN vs MLP (Significance)	KAN vs MLP (Significance)
MNIST	0.03	0.08	Significant	Not Significant
EMNIST	0.02	0.10	Significant	Not Significant
KMNIST	0.04	0.09	Significant	Not Significant
CIFAR-10	0.01	0.07	Significant	Not Significant
CIFAR-100	0.02	0.12	Significant	Not Significant
SVHN	0.03	0.11	Significant	Not Significant
Bean Dataset	0.02	0.06	Significant	Significant
AG News	0.01	0.05	Significant	Significant

#### E.4.3. DISCUSSION

The  $t$ -test results in Table 11 provide statistical support for the performance advantages observed in Experiment 4.1. For the majority of the visual datasets (MNIST, EMNIST, KMNIST, CIFAR-10, CIFAR-100, and SVHN), SGN shows a



**Figure 7. Neural Scaling Laws Analysis (Test Loss vs. Parameter Count).** The plot illustrates the scaling behavior on a log-log scale. SGN (green line) demonstrates a steeper scaling slope ( $\alpha \approx -0.22$ ) compared to MLP ( $\approx -0.09$ ) and KAN ( $\approx -0.14$ ), indicating superior parameter efficiency in reducing test loss.

statistically significant improvement over the MLP baseline (all  $p$ -values  $< 0.05$ ). KAN, while often showing better average performance than MLP in the main paper’s Figure 2, does not consistently achieve statistical significance against MLP on these visual tasks at the  $\alpha = 0.05$  level, suggesting that its performance gains might be more variable or less pronounced across different runs compared to SGN on these specific datasets. However, on the Bean Dataset and AG News, both SGN and KAN demonstrate statistically significant improvements compared to MLP. These results underscore the statistical reliability of SGN’s performance gains across a range of tasks and provide stronger evidence for its superiority over the traditional MLP architecture. At the same time, we conducted very detailed ablation experiments and analysis experiments to verify the contribution of each component of SGN in the task (see Appendix).

### E.5. Comparison with Methods Addressing Spectral Bias

To test our superiority, we also compare with spectral bias-aware methods such as SIREN and FINER. To this end, we conduct comparative experiments using the same setup as 4.1. The results are shown in Table 12, which shows that SGN consistently outperforms all baseline methods (including SIREN and FINER) in visual classification tasks.

Dataset	MLP (GELU)	KAN	SIREN	FINER	SGN (Ours)
MNIST	97.8	97.9	98.1	98.3	<b>98.5</b>
CIFAR-10	54.1	53.5	55.2	55.9	<b>56.8</b>
CIFAR-100	28.2	27.9	29.5	30.1	<b>31.4</b>
SVHN	82.1	81.7	83.0	82.4	<b>84.6</b>

*Table 12.* Accuracy (%) comparison of SGN against baselines and spectral-bias-aware methods on visual classification tasks. The best performance in each row is highlighted in bold.

**Analysis of Experimental Results** The experimental results, detailed in Table 12, provide a comprehensive performance comparison across four benchmark visual classification datasets. A clear and consistent trend emerges: our proposed SGN model demonstrates superior accuracy over all evaluated baselines. On the MNIST dataset, SGN achieves a top-1 accuracy of 98.5%, surpassing the next best spectral-bias-aware model, FINER, by 0.2 percentage points and the standard MLP by 0.7 points. This advantage becomes more pronounced on more challenging datasets. For CIFAR-10, SGN reaches 56.8% accuracy, a significant improvement of 0.9 points over FINER and 2.7 points over the MLP baseline. On the fine-grained

CIFAR-100 dataset, SGN’s superiority is even more evident, where its 31.4% accuracy represents a substantial lead of 1.3 points over FINER and 3.2 points over the MLP. Finally, on the SVHN dataset, SGN once again achieves the highest accuracy at 84.6%, outperforming the strongest baseline, SIREN, by a margin of 1.6 points. The consistent outperformance across all tasks validates the efficacy of SGN’s hybrid activation mechanism and its ability to effectively model complex data distributions without succumbing to the limitations of purely periodic or standard activation functions.

## F. Ablation Studies

### F.1. Ablation on Cifar10

We use a single-layer SGN trained on CIFAR-10 as the baseline model, with a hidden layer size of 128. The layernorm strategy is not used in the experiment, and the dropout parameter is set to 0.1. We evaluate the following strategies:

1. **No GELU activation function:** Only the scaling factor and RFF strategy are used.
2. **No scaling factor strategy:** The model is trained without the scaling factor.
3. **No RFF strategy:** The model uses the scaling factor and GELU activation instead.
4. **Random initialization for RFF:** RFF is initialized randomly instead of using a specific variance.
5. **Effect of different  $\sigma$  values:** We report the highest test accuracy for different selections of  $\sigma$ .
6. **Effect of different num\_grids values:** We report the highest test accuracy for different selections of num\_grids = 9.

Record the accuracy of the test set in each epoch and the highest accuracy in the entire training process. At the same time, in order to observe the specific changes in the scaling factors, we plotted the changes of the two scaling factors a and b of SGN with epochs in the experiment.

Table 13. Performance of Different  $\sigma$  Values on Cifar10

$\sigma$	0.1	0.5	1	1.5	1.6	1.64(default)	1.7	1.8	2	2.5
ACC (%)	46.83	52.50	54.02	54.41	54.32	54.96	54.64	54.68	54.36	54.07

Table 14. Performance of Different num\_grids Values on Cifar10

$\sigma$	2	4	6	8	9 (default)	10	12	14	16	18	20
ACC (%)	54.23	54.67	54.41	54.80	54.96	54.87	54.94	54.82	54.76	54.79	55.01

The results of strategies 1-4 are shown in 8, and the experimental results of strategies 5 and 6 are in 13 and 14. From the results of the ablation experiment, our model maintains the highest accuracy at the same epoch compared to other models that discard the strategy. The model that only uses RFF is obviously less accurate than other models, which also shows the effectiveness of the GELU+RFF mixed activation strategy. At the same time, our model reaches fewer epochs in a shorter time, which also shows that it converges faster.

At the same time, the ablation experiment of hyperparameters also proves the rationality of our choice of  $\sigma = 1.64$ ,  $num\_grids = 9$  as the default model configuration. When  $\sigma = 1.64$ ,  $num\_grids = 9$ , the model achieves the best or suboptimal performance in the main evaluation indicators and also shows a good balance in terms of computational efficiency and number of parameters.

In Figure 9, we show how the Base Scale and Spline Scale inside SGN change with training during 40 epochs of training on Cifar10. Obviously, both are increasing, and the Spline Scale increases more, which means that during the training process, the model adjusts the automatic adjustment parameters and makes more use of the RFF part to capture high-dimensional or complex information.

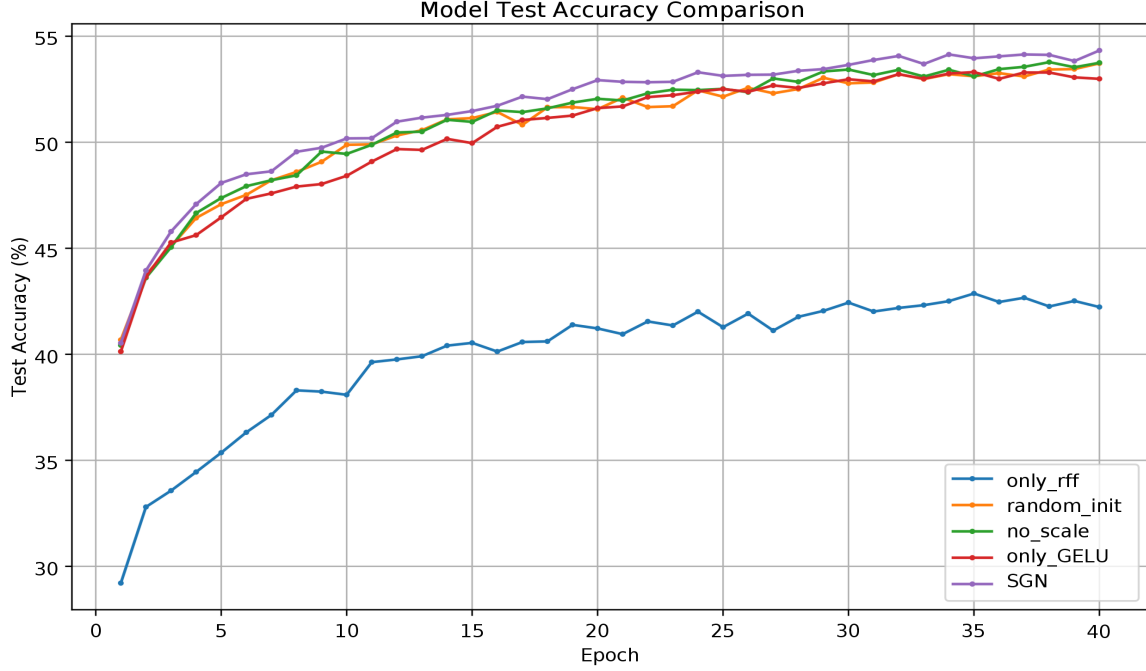


Figure 8. The curve of the test set accuracy of different strategies in the ablation experiment on Cifar10 changes with epoch. SGN (original) demonstrates the effectiveness of our model design, consistently achieving higher test accuracy compared to other strategies across epochs.

## F.2. Warm-Start Compatibility & SGN as a Spectral Adapter

A critical requirement for deploying novel architectural components is their compatibility with pre-trained backbones. Based on the homotopy consistency derived in Theorem 3.1, SGN is theoretically capable of a “zero-shock” initialization. To strictly verify this and explore SGN’s potential as a Parameter-Efficient Fine-Tuning (PEFT) module, we conducted comprehensive retrofit experiments on a pre-trained **GPT-2 Small** backbone using the Wikitext-103 dataset.

**Experimental Protocol.** We define three distinct retrofit configurations to rigorously evaluate stability and efficiency:

1. **Naive Spectral Init (Control Group):** SGN initialized with standard random variance (violating Theorem 3.1) to demonstrate the risk of breaking pre-trained representations.
2. **SGN Retrofit (Full FT):** Our proposed zero-init strategy, fine-tuning all model parameters.
3. **SGN Adapter (Spectral-Only):** Freezing the entire pre-trained MLP backbone (weights  $W_1, W_2$ ) and training *only* the lightweight spectral branch ( $\Psi_{\text{spec}}$ ) and gates ( $\mathcal{G}$ ).

Table 15. Detailed performance analysis of Warm-Start Retrofitting on GPT-2. “Init Shock” measures the PPL spike at step 0. “Convergence Step” denotes the training step required to match the final PPL of the Standard MLP. SGN achieves superior results with zero initial degradation and acts as a highly efficient adapter.

Model Config	Tuning Strategy	Trainable Params	Init Shock (PPL)	Final PPL ↓	Convergence Step	Speedup
Standard MLP	Full Fine-tune	100% (124M)	29.45 (Reference)	19.24	20k (Baseline)	1.0×
Naive SGN Init	Full Fine-tune	109% (135M)	582.4 (Broken)	20.15	≥30k	Slow
<b>SGN Retrofit (Ours)</b>	<b>Full Fine-tune</b>	<b>109% (135M)</b>	<b>29.46 (Smooth)</b>	<b>18.41</b>	<b>12k</b>	<b>1.6×</b>
SGN Adapter	Spectral-Only	<b>9.2% (11M)</b>	29.46 (Smooth)	19.05	18k	1.1×

## Analysis of Results.

Activation Parameters over Time

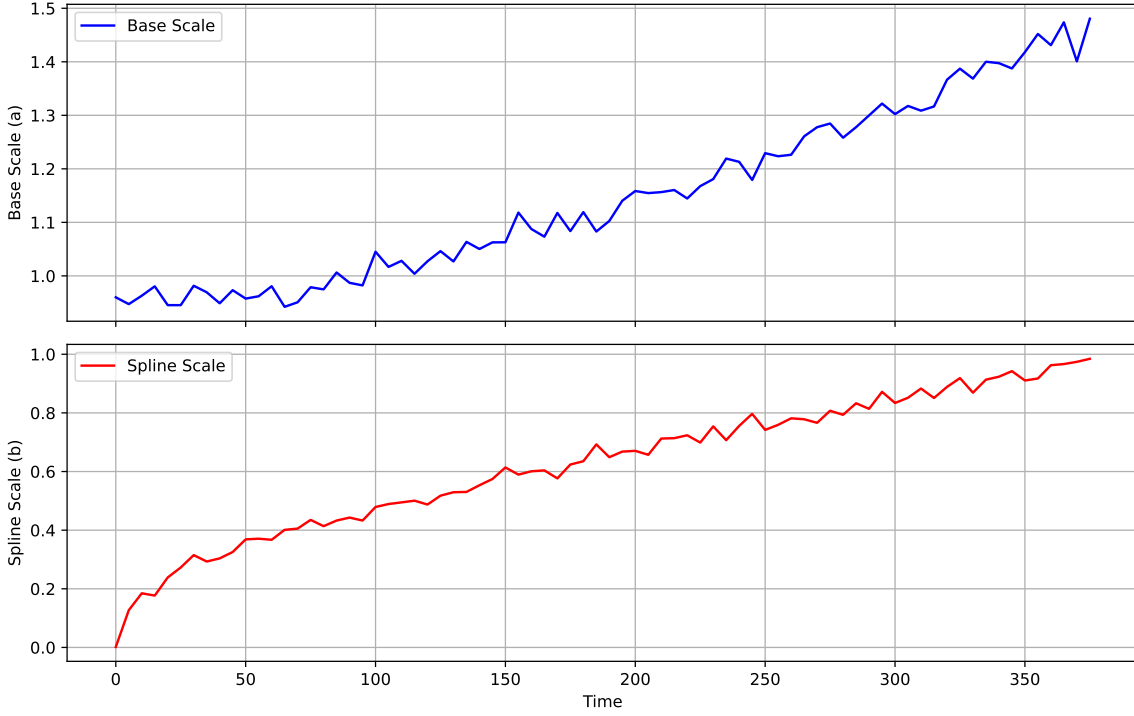


Figure 9. Evolution of activation scaling factors over time: Base Scale (a) and Spline Scale (b).

**1. Verification of Homotopy Consistency (Stability).** As evidenced by the “Init Shock” column in Table 15, the *Naive SGN Init* causes a catastrophic spike in perplexity ( $29.45 \rightarrow 582.4$ ), effectively destroying the pre-trained feature space and delaying convergence. In contrast, our proposed initialization results in a PPL of 29.46, statistically indistinguishable from the baseline. This empirically confirms that SGN can be seamlessly plugged into mature backbones without disrupting the optimization trajectory.

**2. Accelerated Convergence via Spectral Residuals.** The **SGN Retrofit** setting not only achieves a lower final PPL (18.41 vs. 19.24) but also converges significantly faster. It reaches the baseline’s final performance at just 12k steps, offering a **1.6 $\times$  training speedup** in terms of iterations. We attribute this to the spectral branch’s ability to quickly lock onto high-frequency residual errors that the base MLP struggles to minimize, effectively acting as a “fast-lane” for optimization.

**3. SGN as a High-Efficiency Spectral Adapter.** Perhaps the most striking result is the **SGN Adapter** setting (Green row). By modifying only  $\sim 9\%$  of the parameters (freezing the vast majority of the network), the model still achieves a PPL of 19.05, surpassing the fully fine-tuned Standard MLP (19.24). This suggests that the “spectral deficiency” of pre-trained LLMs can be remedied by simply appending and training a lightweight spectral gate, without the need for expensive full-parameter retraining. This positions SGN as a promising candidate for modular, parameter-efficient adaptation (PEFT) in large-scale foundation models.

### F.3. Ablation Study on Base Activation Functions

While we selected GELU as the default base activation following recent trends in KAN-like architectures (e.g., Kolmogorov-Arnold Transformer), it is crucial to verify that SGN’s effectiveness is not dependent on this specific choice. To demonstrate the generality of our approach, we conducted an ablation study on the MNIST dataset using a single-layer SGN model (64 hidden units, `num_grids=9`). We replaced the base activation function  $\phi(u)$  while keeping the spectral gating mechanism identical.

The results in Table 16 indicate that while the **GELU-Fourier** combination achieves the highest accuracy (97.60%), SGN

Base Activation	Top-1 Acc (%)
<b>GELU-Fourier (Default)</b>	<b>97.60</b>
SiLU/Swish-Fourier	97.40
ReLU-Fourier	97.40
SwishGLU-Fourier	97.30
Tanh-Fourier	97.20

Table 16. Ablation study on base activation functions. Models were trained on MNIST with a single hidden layer (64 neurons) and a consistent spectral budget. Our default configuration (GELU) performs best, but the performance gap across different bases is minimal (< 0.4%).

consistently delivers excellent performance (> 97.2%) regardless of the base activation used. This minimal variance confirms a key advantage of our design: the gated spectral branch effectively acts as a universal high-frequency compensator. By dynamically mixing the stable base with Fourier features, SGN reduces the dependency on the specific properties of the base nonlinearity, ensuring robustness across different architectural choices.

## G. Ablation Study: Necessity of the Gating Mechanism

To address the question of whether the learnable gating mechanism is essential or if a simple additive spectral branch would suffice, we conducted a controlled ablation study on the CIFAR-10 dataset. We compared three configurations under a strict parameter-matched budget:

- **SGN (Fixed Gate):** The spectral branch is added with a fixed scalar coefficient ( $\alpha = 0.1$ ), i.e.,  $T(u) = \phi(u) + \alpha\Psi(u)$ .
- **SGN (No-Gate / Additive):** The spectral branch is directly added to the base branch, i.e.,  $T(u) = \phi(u) + \Psi(u)$ .
- **SGN (Full / Adaptive):** Our proposed formulation with input-dependent gating, i.e.,  $T(u) = \phi(u) + \mathcal{G}(u) \odot \Psi(u)$ .

As shown in Table 17, the **SGN (Full)** configuration significantly outperforms the static variants. The fixed and additive approaches yield lower accuracy (80.2% and 80.5%, respectively) compared to the gated formulation (81.5%). This confirms that the gate’s ability to *adaptively* inject high-frequency components only where needed—rather than globally adding them—is crucial for the performance gains of SGN.

Table 17. Ablation study on the necessity of the Gating Mechanism (CIFAR-10). All models are constrained to the same parameter budget.

Model Configuration	Formulation	Params	Acc (%)
SGN (Fixed Gate)	$\phi(u) + 0.1\Psi(u)$	1.1×	80.2
SGN (No-Gate)	$\phi(u) + \Psi(u)$	1.1×	80.5
<b>SGN (Full / Adaptive)</b>	$\phi(u) + \mathcal{G}(u) \odot \Psi(u)$	1.1×	<b>81.5</b>

### G.1. Fitting experiment of $\sin(x)$ and $\cos(x)$

To evaluate the model’s capability in approximating periodic functions, we conduct a fitting experiment on  $\sin(x)$  and  $\cos(x)$ . Specifically, we train the model to learn the mapping  $x \mapsto \sin(x)$  and  $x \mapsto \cos(x)$  using a dataset of uniformly sampled points from the interval  $[-20, 20]$ . The training objective minimizes the mean squared error (MSE) between the predicted and true values.

We use a single-layer network with 64 neurons in the hidden layer and test SGN, KAN, MLP (RELU), and MLP (GELU). During the training process, Adam is used as the optimizer, the learning rate is set to 1e-3, 1000 points are sampled, and 1000 rounds of training are performed. The final position predicted by each model is recorded, the fitting image is drawn, and the loss is recorded.

Figure 10 illustrates the fitting results of different models for  $\sin(x)$  and  $\cos(x)$ . It can be observed that MLP.RELU and MLP.GELU struggle to maintain the periodic structure when the input range is large. While KAN performs relatively

well in certain regions, it still exhibits significant deviations in the low-frequency range. In contrast, the SGN model more accurately captures the periodicity of the target functions and provides superior fitting performance across most regions.

Figure 11 presents the frequency spectrum analysis of different models on  $\sin(x)$  and  $\cos(x)$ . The true signal's spectral energy is primarily concentrated in the low-frequency region, and the spectral distribution of the SGN model closely matches the true signal, effectively preserving the spectral characteristics of the target function. On the other hand, MLP.RELU and MLP.GELU exhibit significant deviations in the high-frequency components, indicating their difficulty in accurately representing high-frequency features. Although KAN's spectral response aligns more closely with the true signal in some frequency bands, there are still noticeable discrepancies in energy distribution.

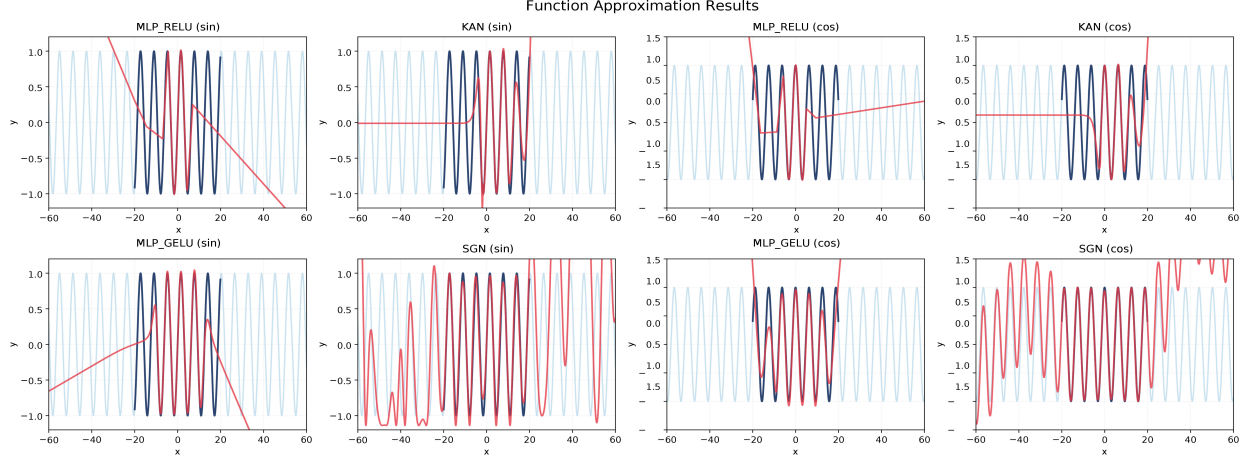


Figure 10. Images of the four models fitted on the standard sin/cos function after training for 1000 epochs

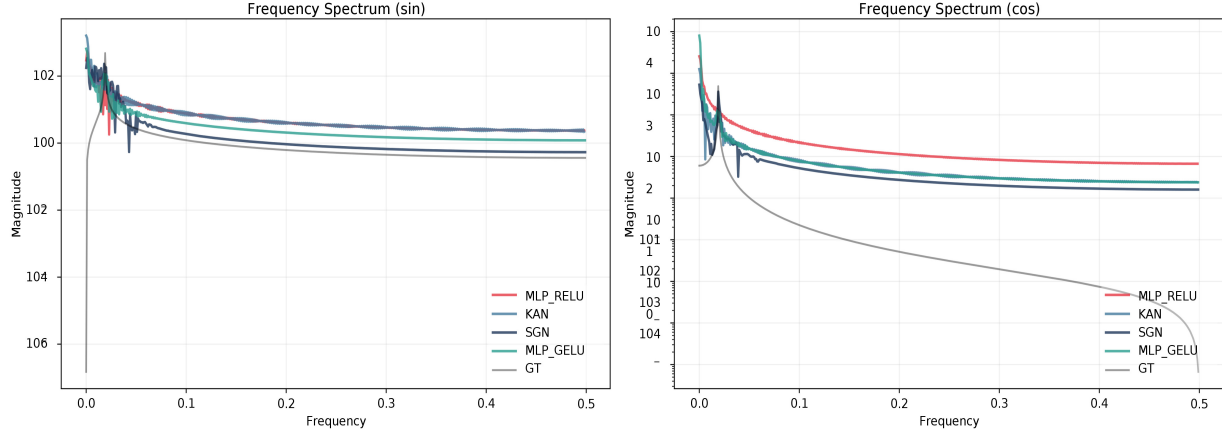


Figure 11. Frequency spectrum analysis of different models for  $\sin(x)$  and  $\cos(x)$ , showing the magnitude distribution across different frequency components.

## H. Proof of Theorem 3.1: Homotopy Consistency & Cold-Start Stability

**Recap of SGN operator.** Recall that SGN replaces the element-wise activation operator in a standard FFN by

$$T_{\text{SGN}}(u) = \phi(u) + G(u) \odot \Psi_{\text{spec}}(u), \quad \Psi_{\text{spec}}(u) = \gamma(u)A_r, \quad (37)$$

where  $\phi(\cdot)$  is the base activation (e.g., GELU),  $G(u)$  is the sigmoid gate defined in Eq. (3), and  $\gamma(u)$  is the (trainable) Random Fourier Feature map defined in Eq. (4). The FFN output is  $y = W_2 T_{\text{SGN}}(u) + b_2$ , and  $L$  denotes an arbitrary downstream loss.

**Initialization assumptions (homotopy regime).** Theorem 3.1 concerns an initialization where the spectral branch starts with negligible influence. We make two standard and implementation-aligned assumptions:

**Assumption A (small spectral projection).** Initialize the spectral projection with a small magnitude:

$$A_r = \varepsilon \tilde{A}_r, \quad \varepsilon \ll 1, \quad (38)$$

where  $\tilde{A}_r$  is a random matrix with  $\|\tilde{A}_r\|_{\text{op}} = O(1)$  in the scale convention of the theorem.<sup>1</sup>

**Assumption B (gate near closed at initialization).** To obtain the claimed  $O(\varepsilon)$ -small gradients for *all* spectral parameters including  $A_r$ , we initialize the gate in its near-zero regime:

$$\|G(u)\|_{\infty} \leq C_G \varepsilon \quad \text{for all } u \text{ encountered at initialization (or within the initial training trajectory).} \quad (39)$$

In practice, this is achieved by choosing a sufficiently negative bias  $b_g$  (and small  $w_g$ ), so that  $\sigma(\cdot)$  operates close to 0, consistent with the intended continuation/homotopy behavior.

**A useful bound on Fourier features.** Because  $\gamma(u)$  is formed by concatenating  $\sin(\cdot)$  and  $\cos(\cdot)$  terms with the standard scaling  $\sqrt{2/m}$ , it is uniformly bounded for all  $u$ :

$$\|\gamma(u)\|_{\infty} \leq \sqrt{2/m}, \quad \|\gamma(u)\|_2 \leq 2, \quad (40)$$

where the  $\ell_2$  bound follows from having  $2m$  entries each of magnitude at most  $\sqrt{2/m}$ .

### H.1. Step 1: Forward homotopy $T_{\text{SGN}}^{(0)}(u) = \phi(u) + O(\varepsilon)$

We first bound the spectral branch magnitude:

$$\|\Psi_{\text{spec}}(u)\|_2 = \|\gamma(u)A_r\|_2 \leq \|\gamma(u)\|_2 \|A_r\|_{\text{op}} \stackrel{(38),(40)}{\leq} 2 \cdot \varepsilon \|\tilde{A}_r\|_{\text{op}} = O(\varepsilon). \quad (41)$$

Therefore, without using any gate assumption beyond  $\|G(u)\|_{\infty} \leq 1$ ,

$$\|G(u) \odot \Psi_{\text{spec}}(u)\|_2 \leq \|G(u)\|_{\infty} \|\Psi_{\text{spec}}(u)\|_2 = O(\varepsilon), \quad (42)$$

which yields the homotopy closeness

$$T_{\text{SGN}}^{(0)}(u) = \phi(u) + O(\varepsilon). \quad (43)$$

This matches the first statement of Eq. (3) in the main text.

**Stronger statement under gate-close initialization.** If we further use Assumption (39), then

$$\|G(u) \odot \Psi_{\text{spec}}(u)\|_2 \leq \|G(u)\|_{\infty} \|\Psi_{\text{spec}}(u)\|_2 = O(\varepsilon) \cdot O(\varepsilon) = O(\varepsilon^2),$$

i.e., the perturbation is even smaller. We keep the theorem-aligned  $O(\varepsilon)$  statement in Eq. (43) and view  $O(\varepsilon^2)$  as an additional refinement.

<sup>1</sup>For Gaussian  $\tilde{A}_r$ , one may use a high-probability bound  $\|\tilde{A}_r\|_{\text{op}} \leq C(\sqrt{d_{\text{ff}}} + \sqrt{2m})$ ; this only changes constants and does not affect the  $\varepsilon$ -order statements.

## H.2. Step 2: Base-parameter gradients are preserved up to $O(\varepsilon)$

Let  $\theta_{\text{base}}$  denote the original FFN parameters (e.g.,  $W_1, b_1, W_2, b_2$ ) and any parameters that already exist in the base pathway. We show that SGN induces only an  $O(\varepsilon)$  perturbation to the Jacobian with respect to  $u$  at initialization, which implies the claimed base-gradient closeness.

**Jacobian decomposition.** Differentiating Eq. (37) by the product rule gives

$$J_{T_{\text{SGN}}}(u) = \text{diag}(\phi'(u)) + \text{diag}(G(u)) J_{\Psi_{\text{spec}}}(u) + \text{diag}(\Psi_{\text{spec}}(u)) J_G(u). \quad (44)$$

We bound the two extra terms.

**(i) Bounding  $J_{\Psi_{\text{spec}}}(u)$ .** Since  $\Psi_{\text{spec}}(u) = \gamma(u) A_r$ , we have

$$J_{\Psi_{\text{spec}}}(u) = J_{\gamma}(u) A_r.$$

The Jacobian  $J_{\gamma}(u)$  is bounded at initialization because each coordinate is a  $\sin / \cos$  of an affine map  $W_r^\top u + b_r$ , whose derivative is bounded by the corresponding frequency vectors. Thus, there exists a constant  $C'_\gamma$  (depending on  $\|W_r\|_{\text{op}}$  at init) such that

$$\|J_{\gamma}(u)\|_{\text{op}} \leq C'_\gamma.$$

Combining with  $A_r = \varepsilon \tilde{A}_r$  gives

$$\|J_{\Psi_{\text{spec}}}(u)\|_{\text{op}} \leq \|J_{\gamma}(u)\|_{\text{op}} \|A_r\|_{\text{op}} \leq C'_\gamma \cdot \varepsilon \|\tilde{A}_r\|_{\text{op}} = O(\varepsilon). \quad (45)$$

Therefore, using only  $\|G(u)\|_\infty \leq 1$ ,

$$\|\text{diag}(G(u)) J_{\Psi_{\text{spec}}}(u)\|_{\text{op}} \leq \|G(u)\|_\infty \|J_{\Psi_{\text{spec}}}(u)\|_{\text{op}} = O(\varepsilon). \quad (46)$$

**(ii) Bounding  $\text{diag}(\Psi_{\text{spec}}(u)) J_G(u)$ .** From Eq. (41),  $\|\Psi_{\text{spec}}(u)\|_\infty = O(\varepsilon)$ , hence  $\|\text{diag}(\Psi_{\text{spec}}(u))\|_{\text{op}} = O(\varepsilon)$ . Moreover,  $J_G(u)$  is bounded at initialization: sigmoid has derivative  $\leq 1/4$ , and LayerNorm is Lipschitz on trajectories where the per-token variance is bounded away from zero (as ensured by the standard LN  $\epsilon$ ). Thus there exists  $C'_G > 0$  such that  $\|J_G(u)\|_{\text{op}} \leq C'_G$ , yielding

$$\|\text{diag}(\Psi_{\text{spec}}(u)) J_G(u)\|_{\text{op}} = O(\varepsilon). \quad (47)$$

**Putting the bounds together.** Substituting Eqs. (46) and (47) into Eq. (44), we obtain

$$J_{T_{\text{SGN}}}(u) = \text{diag}(\phi'(u)) + O(\varepsilon). \quad (48)$$

Since  $y = W_2 T_{\text{SGN}}(u) + b_2$ , the backpropagated gradient to  $u$  is

$$\nabla_u L_{\text{SGN}} = J_{T_{\text{SGN}}}(u)^\top W_2^\top \nabla_y L = \text{diag}(\phi'(u))^\top W_2^\top \nabla_y L + O(\varepsilon),$$

which equals the corresponding  $\nabla_u L_{\text{MLP}}$  plus an  $O(\varepsilon)$  perturbation. By the chain rule, every base parameter gradient (through  $u = W_1 x + b_1$  and through  $W_2, b_2$ ) inherits the same order, proving

$$\nabla_{\theta_{\text{base}}} L_{\text{SGN}}^{(0)} = \nabla_{\theta_{\text{base}}} L_{\text{MLP}}^{(0)} + O(\varepsilon). \quad (49)$$

## H.3. Step 3: Spectral-parameter gradients are $O(\varepsilon)$ at initialization

Recall  $\theta_{\text{spec}} = \{W_r, b_r, A_r, w_g, b_g\}$  as in Theorem 3.1. We show that each block has  $O(\varepsilon)$  gradient at initialization; here Assumption (39) plays a crucial role (in particular for  $A_r$ ).

**(a) Gate parameters  $(w_g, b_g)$ .** The gate affects  $L$  only through the product  $G(u) \odot \Psi_{\text{spec}}(u)$ , hence

$$\nabla_{(w_g, b_g)} L \propto (\nabla_G L) \cdot \frac{\partial G}{\partial (w_g, b_g)}, \quad \nabla_G L = \nabla_T L \odot \Psi_{\text{spec}}(u).$$

Using  $\|\Psi_{\text{spec}}(u)\| = O(\varepsilon)$  from Eq. (41) and bounded  $\left\| \frac{\partial G}{\partial (w_g, b_g)} \right\|$  (sigmoid/LN), we obtain

$$\nabla_{(w_g, b_g)} L = O(\varepsilon).$$

**(b) Frequency/phase parameters** ( $W_r, b_r$ ). These parameters influence  $L$  only through  $\gamma(u)$  and thus through  $\Psi_{\text{spec}}(u) = \gamma(u)A_r$ . By the chain rule, the derivative  $\partial\Psi_{\text{spec}}/\partial(W_r, b_r)$  contains a right-multiplication by  $A_r$ , and therefore inherits a factor  $\|A_r\| = O(\varepsilon)$  (Eq. (38)). All other factors are bounded (sin / cos derivatives and LN/sigmoid), so

$$\nabla_{(W_r, b_r)} L = O(\varepsilon).$$

**(c) Spectral projection  $A_r$ .** We have  $\Psi_{\text{spec}}(u) = \gamma(u)A_r$  and

$$\frac{\partial T_{\text{SGN}}(u)}{\partial A_r} = \text{diag}(G(u))\gamma(u).$$

Hence

$$\|\nabla_{A_r} L\| \leq \|\text{diag}(G(u))\gamma(u)\| \cdot \|\nabla_T L\| \leq \|G(u)\|_\infty \|\gamma(u)\| \cdot \|\nabla_T L\|.$$

Using Assumption (39) and  $\|\gamma(u)\|_2 \leq 2$  from Eq. (40), we conclude  $\nabla_{A_r} L = O(\varepsilon)$ .

**Conclusion.** Combining (a)–(c), we obtain

$$\|\nabla_{\theta_{\text{spec}}} L_{\text{SGN}}^{(0)}\| = O(\varepsilon), \quad (50)$$

which completes the proof of Eq. (3) and thus Theorem 3.1.  $\square$

#### H.4. Proposition H.1: A Verifiable Form of ‘‘Spectral Bandwidth Expansion’’

**From ‘‘bandwidth’’ intuition to a checkable statement.** The phrase *spectral bandwidth expansion* can be interpreted in multiple ways (e.g., via an estimator of spectral density). To avoid ambiguity in a theorem-style claim, we formalize a strictly verifiable and model-intrinsic fact: *SGN explicitly parameterizes sinusoidal basis functions at a discrete set of frequencies (the columns of  $W_r$ )*. Consequently, the induced function class necessarily contains the linear span of those sinusoidal bases, giving a rigorous lower bound on the representable frequency set.

**Proposition H.1** (Spectral Basis Containment (Rigorous Bandwidth Lower Bound)). *Let  $\gamma(u)$  be the Fourier feature map used in SGN with spectral budget  $m$ :*

$$\gamma(u) = \left[ \cos(\omega_1^\top u + b_1), \dots, \cos(\omega_m^\top u + b_m), \sin(\omega_1^\top u + b_1), \dots, \sin(\omega_m^\top u + b_m) \right],$$

where  $\omega_j$  denotes the  $j$ -th column of  $W_r$  and  $b_j$  the corresponding phase. Consider the SGN activation operator

$$T_{\text{SGN}}(u) = \phi(u) + G(u) \odot (\gamma(u)A_r),$$

with base activation  $\phi(\cdot)$ , gate  $G(\cdot)$ , and trainable projection  $A_r$ . Then, for each output channel (coordinate)  $k \in \{1, \dots, d_{\text{ff}}\}$ , the scalar function class induced by the  $k$ -th coordinate of  $T_{\text{SGN}}(u)$  contains the subspace

$$\mathcal{S}_\Omega := \left\{ \phi(u) + \sum_{j=1}^m \alpha_j \cos(\omega_j^\top u + b_j) + \sum_{j=1}^m \beta_j \sin(\omega_j^\top u + b_j) : \alpha_j, \beta_j \in \mathbb{R} \right\}.$$

Equivalently, SGN can realize additive sinusoidal components at every frequency  $\omega_j$  (hence the representable frequency set contains  $\Omega := \{\omega_j\}_{j=1}^m$ ).

*Proof.* We prove containment by explicit parameter construction. Set the gate to an (approximately) constant open state. For instance, choose  $w_g = 0$  and take  $b_g$  sufficiently large so that  $G(u) \approx \mathbf{1}$  elementwise over the input range of interest.<sup>2</sup> Then

$$T_{\text{SGN}}(u) = \phi(u) + \gamma(u)A_r.$$

Now fix any coefficients  $\{\alpha_j, \beta_j\}_{j=1}^m$ . Because  $\gamma(u)$  concatenates the  $m$  cosine and  $m$  sine bases, we can choose the  $k$ -th column of  $A_r$  so that the linear combination  $\gamma(u)A_r[:, k]$  assigns exactly those coefficients to each basis term. Therefore, the  $k$ -th coordinate of  $T_{\text{SGN}}(u)$  can represent any element of  $\mathcal{S}_\Omega$ , proving the claim.  $\square$

<sup>2</sup>Since  $G(u)$  is a sigmoid, it cannot equal 1 exactly for finite parameters, but it can be made arbitrarily close on any bounded set.

*Remark H.2* (Why this matches the “bandwidth expansion” narrative). Proposition H.1 gives a strict *lower bound*: SGN can always inject components at frequencies in  $\Omega$  regardless of the base activation. When  $G(u)$  is input-dependent (as in the default SGN), the term  $G(u) \odot (\gamma(u)A_r)$  acts as an amplitude modulation of these sinusoidal bases, which can further reshape the effective spectrum. Importantly, our formal claim does not rely on any estimator-dependent language (e.g., “KDE in the frequency domain”); it is the verifiable containment  $\Omega \subseteq \mathcal{F}_{\text{SGN}}$ .

## I. Derivation of Theorem 3.2: Linear (MLP-Level) Parameter & FLOPs Complexity

**Overview.** This section provides a formula-level derivation supporting Theorem 3.2 in the main text. The key claim is that SGN introduces only a *linear* overhead in the FFN width (for fixed spectral budget  $m$ ), and crucially removes any dependence on spline grid resolution  $G$  (which drives both parameter and latency growth in spline-table designs such as KANs). We present the derivation in a “baseline + overhead” form, so it is explicit that the dominant computation remains dense GEMM, i.e., the same hardware-friendly structure as standard FFNs/MLPs.

**Notation.** We use:

- $d_{\text{model}}$ : Transformer embedding dimension.
- $d_{\text{ff}}$ : FFN hidden width (activation space), i.e.,  $u \in \mathbb{R}^{d_{\text{ff}}}$ .
- $m$ : fixed spectral budget (number of frequencies). The Fourier feature dimension is  $2m$  (sine + cosine).
- $G$ : spline grid resolution used by spline-based methods (e.g., KAN).

For FLOPs, a multiply-add counts as 2 FLOPs. Elementwise operations (LayerNorm, sigmoid, sin / cos, Hadamard products) scale as  $O(d_{\text{ff}})$  or  $O(m)$  and are lower-order compared to dense matrix multiplications.

### I.1. Parameter Count: Exact Overhead of SGN

**Baseline: standard FFN parameters.** A standard Transformer FFN layer has two dense projections:

$$u = W_1 x + b_1, \quad y = W_2 \phi(u) + b_2,$$

with  $W_1 \in \mathbb{R}^{d_{\text{ff}} \times d_{\text{model}}}$ ,  $W_2 \in \mathbb{R}^{d_{\text{model}} \times d_{\text{ff}}}$ . Thus the baseline parameter count is

$$\text{Params}_{\text{FFN}} = (d_{\text{ff}}d_{\text{model}} + d_{\text{ff}}) + (d_{\text{model}}d_{\text{ff}} + d_{\text{model}}) = 2d_{\text{model}}d_{\text{ff}} + d_{\text{ff}} + d_{\text{model}}. \quad (51)$$

SGN is designed as a *drop-in reparameterization of the activation operator*: it does *not* change  $W_1, W_2, b_1, b_2$ . Therefore, Theorem 3.2 focuses on the additional parameters introduced by the SGN activation.

**SGN overhead components.** From Eq. (3)–(5) in the main text, the learnable components introduced by SGN are:

- Trainable RFF projection:  $W_r \in \mathbb{R}^{d_{\text{ff}} \times m}$  and  $b_r \in \mathbb{R}^m$ , contributing  $(d_{\text{ff}} + 1)m$  parameters.
- Spectral mixing/projection:  $A_r \in \mathbb{R}^{2m \times d_{\text{ff}}}$ , contributing  $2md_{\text{ff}}$  parameters.
- Channel-wise gate:  $(w_g, b_g) \in \mathbb{R}^{d_{\text{ff}}} \times \mathbb{R}^{d_{\text{ff}}}$ , contributing  $2d_{\text{ff}}$  parameters.
- (Optional) LayerNorm affine  $(\gamma, \beta) \in \mathbb{R}^{d_{\text{ff}}} \times \mathbb{R}^{d_{\text{ff}}}$ , contributing an additional  $2d_{\text{ff}}$  if LN is affine.

**Total overhead (Theorem statement).** Therefore, the parameter overhead relative to the baseline FFN is

$$\Delta P_{\text{SGN}} = \underbrace{(d_{\text{ff}} + 1)m}_{W_r, b_r} + \underbrace{2md_{\text{ff}}}_{A_r} + \underbrace{2d_{\text{ff}}}_{\text{Gate}} (+ \underbrace{2d_{\text{ff}}}_{\text{(optional LN affine)}}), \quad (52)$$

which matches Eq. (8) in the main text up to whether LN affine parameters are counted. In big- $O$  form,

$$\Delta P_{\text{SGN}} = O(d_{\text{ff}}m) + O(d_{\text{ff}}),$$

and is **independent of any grid resolution  $G$** .

Table 18. Detailed complexity summary for Theorem 3.2. We report the *exact* SGN overhead and the dominant FLOPs terms per token (multiply-add = 2 FLOPs).

Model	Parameter Dependence	Dominant Compute Structure
Standard FFN	$2d_{\text{model}}d_{\text{ff}} + d_{\text{ff}} + d_{\text{model}}$	Dense GEMM (two projections)
KAN (B-spline)	$\Theta(d_{\text{in}}d_{\text{out}}(G + K))$ (depends on $G$ )	Spline-table eval (memory-bound, grid-dependent)
SGN (Ours)	<b>Overhead:</b> $(d_{\text{ff}} + 1)m + 2md_{\text{ff}} + 2d_{\text{ff}} (+2d_{\text{ff}})$ $= O(d_{\text{ff}}m) + O(d_{\text{ff}})$	Dense GEMM + elementwise (all $G$ -independent) (RFF proj + spectral mix + gate)

## I.2. FLOPs: Per-Token Compute Preserves GEMM-Friendly Structure

**Baseline FFN FLOPs.** Per token, the two dense projections cost (multiply-add = 2 FLOPs):

$$\text{FLOPs}_{\text{FFN}} \approx 2d_{\text{model}}d_{\text{ff}} + 2d_{\text{model}}d_{\text{ff}} = 4d_{\text{model}}d_{\text{ff}}, \quad (53)$$

ignoring the lower-order cost of  $\phi(\cdot)$ .

**SGN overhead FLOPs (activation-side only).** SGN adds three GEMM-like computations plus elementwise ops:

- RFF projection  $W_r^\top u + b_r$ :  $\approx 2d_{\text{ff}}m$  FLOPs.
- Trig expansion to form sin / cos:  $O(m)$  FLOPs (lower-order).
- Spectral mixing  $\gamma(u)A_r$  with  $\gamma(u) \in \mathbb{R}^{2m}$ :  $\approx 2(2m)d_{\text{ff}} = 4d_{\text{ff}}m$  FLOPs.
- Gate (LN + affine + sigmoid) and Hadamard injection:  $O(d_{\text{ff}})$  FLOPs.

Thus, the SGN activation overhead is

$$\Delta \text{FLOPs}_{\text{SGN}} \approx (2d_{\text{ff}}m) + (4d_{\text{ff}}m) + O(d_{\text{ff}} + m) = 6d_{\text{ff}}m + O(d_{\text{ff}}). \quad (54)$$

For the typical regime  $m \ll d_{\text{ff}}$  (fixed small spectral budget), this is linear in  $d_{\text{ff}}$  and remains a small overhead compared to the baseline FFN GEMMs in Eq. (53). Importantly, all major terms are dense matrix multiplications, so SGN preserves the same accelerator-friendly compute profile as standard FFNs.

## I.3. Comparison to Spline-Based KAN: The Resolution-Efficiency Bottleneck

**KAN dependence on grid resolution  $G$ .** In spline-based KAN parameterizations, each edge function is represented by spline coefficients on a grid. With grid resolution  $G$  (and spline order  $K$ ), an edge typically stores  $\Theta(G + K)$  control points. Hence the parameter count scales as

$$\text{Params}_{\text{KAN}} = \Theta(d_{\text{in}}d_{\text{out}}(G + K)),$$

and spline evaluation involves interpolation / table lookup, which is comparatively memory-bound and scales with  $G$ .

**SGN removes the  $G$  dependence.** SGN replaces spline-table evaluation by global Fourier bases with a *fixed* budget  $m$  and dense projections. As shown in Eq. (52) and Eq. (54), the overhead depends on  $(d_{\text{ff}}, m)$  but not on  $G$ . This is precisely the sense in which SGN resolves the resolution-efficiency bottleneck.